For Reference

NOT TO BE TAKEN FROM THIS ROOM

Ex libris
Universitatis
Albertaensis

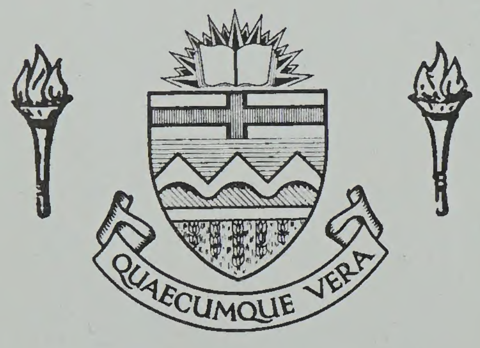

QUAECUMQUE VERA

Digitized by the Internet Archive
in 2020 with funding from
University of Alberta Libraries

https://archive.org/details/Zimanyi1970

THE UNIVERSITY OF ALBERTA

DYNAMIC PROCESSES AND STABILITY OF PLASMA DISCHARGES IN LIQUIDS

by

© [illegible] KIMANYI

A THESIS
SUBMITTED TO THE FACULTY OF GRADUATE STUDIES
IN PARTIAL FULFILMENT OF THE REQUIREMENTS FOR THE DEGREE
OF MASTER OF SCIENCE

DEPARTMENT OF ELECTRICAL ENGINEERING

EDMONTON, ALBERTA
FALL, 1970

THE UNIVERSITY OF ALBERTA

DYNAMIC PROCESSES AND STABILITY OF PLASMA DISCHARGES IN LIQUIDS

by

© JAN ZIMANYI

A THESIS
SUBMITTED TO THE FACULTY OF GRADUATE STUDIES
IN PARTIAL FULFILMENT OF THE REQUIREMENTS FOR THE DEGREE
OF MASTER OF SCIENCE

DEPARTMENT OF ELECTRICAL ENGINEERING

EDMONTON, ALBERTA

FALL, 1970

Thesis
1974F
223

UNIVERSITY OF ALBERTA

FACULTY OF GRADUATE STUDIES

The undersigned certify that they have read, and recommend to the Faculty of Graduate Studies for acceptance, a thesis entitled "Dynamic Processes and Stability of Plasma Discharges in Liquids", submitted by Jan Zimanyi in partial fulfilment of the requirements for the degree of Master of Science.

ABSTRACT

The dynamic processes and stability of plasma discharges in the intermediate range between the spark and the arc type of discharge in liquid dielectrics are examined. The object of this investigation is the industrial application of this type of discharge, in particular electro-discharge machining. Available information about this topic is assembled and discussed. In particular the low frequency liquid oscillations, their damping and thermal instabilities are investigated.

The results of experiments performed to investigate the properties of discharges in water and other liquid dielectrics are presented. A discussion of experimental and theoretical results with respect to practical application is given.

ACKNOWLEDGEMENTS

The author wishes to express his thanks to Dr. C.E. Capjack who supervised this project. The many valuable discussions and checking on many equations contributed to completion.

The author also wishes to thank the National Research Council of Canada and the Department of Electrical Engineering, University of Alberta, for financial support during this work.

Acknowledgement is also extended to the staff members and postgraduate students of the Department of Electrical Engineering for their suggestions and cooperation.

TABLE OF CONTENTS

Page

Chapter 1. INTRODUCTION 1

1.1 Industrial applications of the plasma discharges in liquids 1
1.2 Spark and arc discharges 2
1.3 Importance of discharge instabilities in EDM 5

Chapter 2. DYNAMICS OF THE STABLE DISCHARGE IN A LIQUID 8

2.1 Plasma channel created by a spark discharge in a liquid 8
2.2 The steady plasma column of a discharge in a liquid 10
2.3 Oscillation of the gas bubble 13
2.4 The frictional losses of a cylindrical bubble oscillation 20
2.5 Dissociation of the water vapours 29
2.6 Ionization and thermal conductivity of the water vapours 32

Chapter 3. INSTABILITY OF THE PLASMA COLUMN 40

3.1 Unstable electrode phenomena 40
3.2 Unstable column phenomena 41
3.3 Other unstable phenomena 44
3.4 Correction of the thermal instability condition 45
3.5 Summary 47

Chapter 4. EXPERIMENTAL RESULTS 49

4.1 Apparatus description and method of measurement 49
4.2 Liquid and electrode material used 51
4.3 Experimental data 53

Chapter 5. DISCUSSION AND SUMMARY 63

5.1 Discussion of theoretical investigations 63
5.2 Discussion of the experimental data and comparison with theory 64
5.3 Summary 66

BIBLIOGRAPHY 67

Appendix DESCRIPTION OF THE IMPULSE GENERATOR 70

LIST OF FIGURES

Figure Page

1.1 The working principle of the relaxation EDM generator 3

1.2 The working principle of the independent EDM generator 3

2.1 The cylindrical discharge model with temperature T and density ρ distribution 10

2.2 (a) Typical change of the radial gas temperature distribution, (b) Dependence of the axial gas temperature T_c on pressure p current I and radius R (After Ecker and Zoller[18]) 12

2.3 The oscillating cylindrical bubble 13

2.4 The dependence of radius R on time t for an oscillating cylindrical bubble in water 17

2.5 The dependence of R/R_1 on $t/\sqrt{\rho\ 3/2}\ R$ for a spherical bubble in water 17

2.6 The measured and calculated values of radius R of an oscillating cylindrical bubble in water 18

2.7 The dependence of R_3/R_1 on pressure p_1 for a spherical bubble in water for various values of γ. 19

2.8 The viscous flow around the oscillating cylindrical bubble 21

2.9 The segment of the moving annulus and its surface element 23

2.10 The dependence of radii R and r*, and frictional losses W for an oscillating cylindrical bubble in water 28

2.11 The dependence of $\log_{10}K$ for reactions
(A) $H_2O \rightleftarrows H_2 + O_2/2$
(B) $H_2 \rightleftarrows 2H$
(C) $O_2/2 \rightleftarrows O$ 33

2.12 The dependence of equilibrium constant ε on temperature T at pressure 1 atm for reactions
(A) $H_2O \rightleftarrows H_2 + O_2/2$
(B) $H_2 \rightleftarrows 2H$
(C) $O_2/2 \rightleftarrows O$ at 1 atmosphere pressure 34

2.13 The temperature T and the thermal conductivity κ in a gas shell 39

Figure Page

3.1 Records of discharges in liquids made by a time resolving camera 42

3.2 The dependence of I_{cr} on I for (a) σ = const (b) $\sigma \neq$ const 46

4.1 The shapes of electrodes 53

4.2 The measured time dependence of U and I 53

4.3 The dependence I_{ac} on I_{dc} for different electrode distances 55

4.4 The dependence of I_{ac} on I_{dc} for various values of R_L 56

4.5 The dependence of U_{dc} on I_{dc} for various values of d 57

4.6 The dependence of U_{dc} on the electrode distance d for different R_L 58

4.7 The dependence of I_{ac} on I_{dc} for water, nitrogen, hexane, benzene and silicon oil 60

4.8 The dependence of I_{ac} on I_{dc} for various Cu-W electrode combinations 61

A.1 Schematic diagram for the impulse generator 71

LIST OF SYMBOLS

$A = \frac{10}{E} \lambda_{oo} T_{oo}$

C	capacity
d	Electrode distance
E	electric field
EDM	electro-discharge machining
F	force
I	electric current
I_{ac}	ac component of the discharge current
I_{dc}	dc component of the discharge current
K	equilibrium constant
k	Boltzmann constant
n	particle density
P	pressure
$\dot{Q}$	heat flow rate
R	radius of bubble
R_L	loading resistor
r	radius
S(T)	right hand side of the Saha equation
T	temperature
T_{oo}	temperature within Shottky approximation
t	time
U	voltage, velocity
U_o	power source voltage
U_{ac}	ac component of the discharge voltage
U_{dc}	dc component of the discharge voltage

U_R	radial velocity of the gas bubble
w	energy
β =	$\frac{1}{I\Omega_i}$
γ	specific heat ratio
δ	boundary layer thickness
ε	degree of reaction
ϕ	velocity potential
κ	heat conductivity
λ_{oo}	heat conductivity within Shottky approximation
μ	viscosity
Ω_o	outer circuit resistance
Ω_i	discharge resistance
ρ	density
σ =	$\frac{1}{1 + \frac{\Omega_i}{\Omega_o}}$
τ	time constant

CHAPTER 1

INTRODUCTION

1.1 Industrial applications of plasma discharges in liquids

Plasma discharges have been employed in many branches of industry for many years. Probably the best known is the high pressure arc burning in a gas. The high temperature of its plasma column lends itself to welding, lighting and in metallurgical processes.

Other industrial applications for the electrical discharge have been found in the past 30 years. In particular, discharges in liquids which are convenient for many technological operations have been used. These can be divided in three main groups:

i) electro-discharge machining (EDM)

ii) electro-hydraulical effect (EHE) - production of powerful shock waves whose applications include the forming of metal plates and the disintegration of minerals.

iii) plasma torches - used for metal cutting, surfacing, chemical synthesis, etc.

At present, the most widely used technology of the above three groups is EDM. The principle of this method consists of an errosion effect caused by the spark (or not purely spark) discharge on the electrode surfaces in the liquid. The discharge burns between two electrodes in a gap about 0.05 to 0.2 mm wide normally filled with a liquid dielectric such as water or oil. Values for the discharge duration range from 1 to 1000 μsecs. Many changes in the liquid and

on the electrode surfaces may be observed after the discharge extinguishes. The most important change is the creation of a crater on the electrode surface. Under certain conditions the volume ratio of the two electrode craters may extend from 1:1 to 1:1000. Through the use of a large number of discharges a machining process is obtained where the electrode with the smaller craters is a tool and the electrode with the larger craters is the workpiece.

1.2 Spark and arc discharges

The basic difference between the spark and the arc discharge lies in the dynamics of the two phenomena. The arc is a steady plasma discharge with no considerable instabilities. A spark on the other hand is a very dynamic discharge, changing its geometry, temperature, pressure and composition on a very short term scale, typically several hundred nanoseconds. A spark is often the initial state of the arc discharge. A very rapid expansion of the plasma channel is a typical characteristic of a spark.

The velocity of this expansion is greatest in the initial state and reaches values of several hundred meters per second. The velocity of the initial expansion of the plasma channel is therefore supersonic and is accompanied by one or more shock waves. While the overpressure inside the arc column is very small (few centimeters of the water column), the spark overpressure is very high and can reach several ten thousand atm. of pressure in the liquid environment. The high overpressure is obviously connected with different temperatures inside the discharge channel. The temperature inside the spark discharge channel is considerably higher than that inside the arc discharge

assuming that both discharges occur under equal conditions.

The original EDM machines employed only a spark discharge. The spark discharge was driven from a so called relaxation generator shown in Figure (1.1).

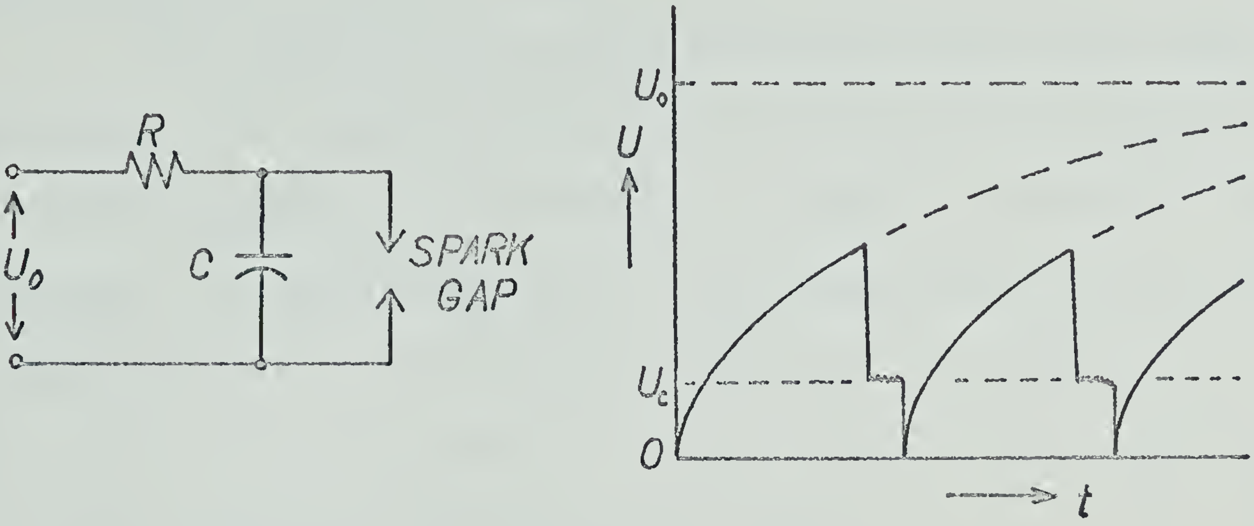

Fig. (1.1) The working principle of the relaxation EDM generator.

The capacitor C is charged from the power source through resistor R and is discharged into the spark gap after the voltage on the capacitor is sufficiently high for liquid breakdown to occur. The low inductive connection between the capacitor C and the spark gap allows a very short high amplitude current discharge.

The modern generators (so called independent generators) with more flexible parameters are able to provide impulses of the type shown in Figure (1.2)

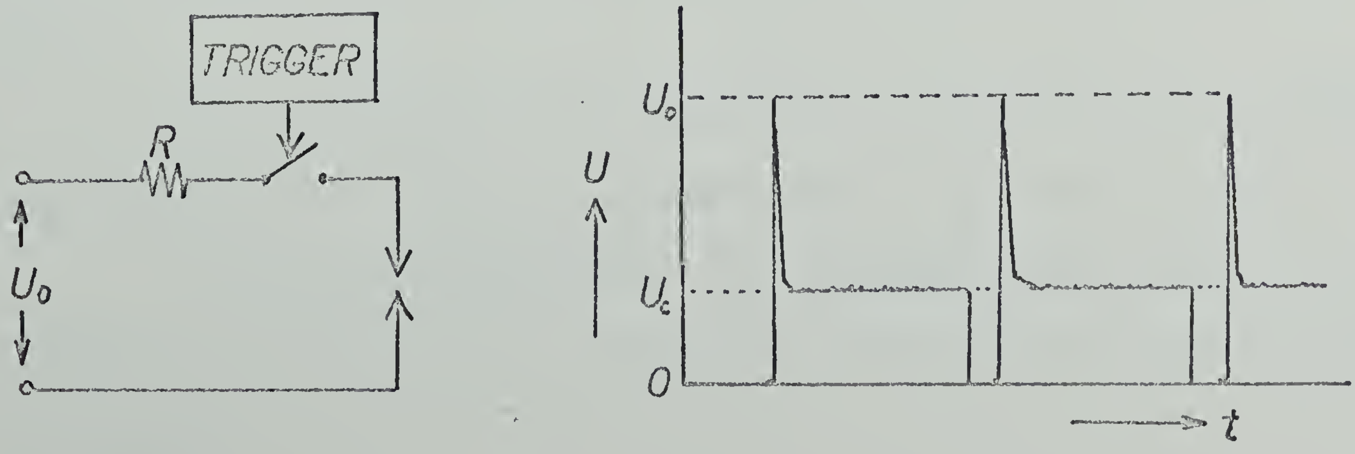

Fig. (1.2) The working principle of the independent EDM generator.

By using a triggered switching element, current impulses (usually rectangularly shaped) with an amplitude less than that depicted in fig. (1.1) may be obtained. The length of such impulses may reach several hundreds μsecs.

The independent generators do not work with purely spark discharges. The supersonic expansion lasts only a very short time at the very beginning of the discharge. During the remainder of the discharge, the expansion velocity is below supersonic and the high overpressure typical of a spark no longer exists. However, the depression and sometimes also the channel contraction not typical of an arc-like steady discharge may still exist.

Therefore this kind of discharge may be divided in three phases. The first phase is the spark-like behaviour, the second an intermediate subsonic expansion and the third an arc-like burning under changing outer conditions.

For EDM, the first and third phases of the discharge are of most importance. The first phase is of importance because of the high temperature inside the plasma channel and the strong shock waves propagating from the discharge. The third phase is important because the discharge is in this phase for an essential part of the discharge time.

The life time of the second phase is relatively short, making this portion of the discharge insignificant in the study of EDM.

Thus the investigation of the independent EDM generator discharges may be separated into the study of the spark-like and the arc-like phases.

The first spark-like phase in which a relatively small amount of energy is released is a rather complicated problem and will not be discussed in this thesis. The influence of the first and second phases on the third will be discussed only.

1.3 Importance of discharge instabilities in EDM

Steady discharges with the released energy preserved by using the minimum possible current amplitude are suited to many EDM operations. However, the lowering of the current amplitude is limited by the discharge instabilities which are considerably enhanced at small current amplitudes. Any changes in the shape, position and magnitude of the discharge channel is for technological reasons undesirable because according to experimental data these are connected with the tool electrode damage. This damage is probably caused by shock or other mechanical waves which accompany the plasma column instabilities, hitting the overheated and melted electrode surface. This results in pieces being torn out of the electrode material.

It is known that under certain outer conditions it is possible to operate with very small current amplitudes without any sensible instabilities. On the other hand with some different technological operations, instabilities are observed with much higher current amplitudes. Thus the instabilities may be influenced by outer conditions. The instabilities are manifested in the outer electrical circuitry as changes in the discharge current.

If the instabilities are sufficiently intense and the current amplitude sufficiently small, discharge interruption can occur. From the technological point of view this is the worst case, because each

interruption implies a new start of discharge with the additional undesirable spark-like discharge phase.

A complete theoretical description of the type of discharge discussed above has not been done yet. The theory describing a pure spark discharge is satisfactorily developed and is successfully applied in the relaxation generator EDM theory. The theory of the stable high pressure arc discharge is also well developed. The results of the theory on pure spark discharges and the theory on high pressure arc discharges may be used as a basis for developing a more detailed theoretical and experimental investigation of the independent EDM discharges. A complete study of the discharge instabilities is a rather complex problem. An instability may develop for several reasons, in addition the coexistence of several kinds of instabilities can not be excluded.

In addition many instabilities as described in publications, still await a theoretical description, eg. Hoyaux[1], Kocian[2].

The important unknowns in the independent generator EDM method are the magnitude of the pressure and temperature in the discharge space during and after the discharge and the origin and state of the discharge channel instabilities. These problems can not be exactly theoretically solved. An exact theoretical solution for these unknowns is not possible due to the complexity of the phenomena involved. Some simplification in the theoretical description of the discharge is necessary if an approximate solution is to be obtained. An experimental verification of the simplifying assumptions must then be carefully made. Similarly all experimental data should be properly theoretically explained.

In this thesis, contemporary knowledge about important phenomena occurring in plasma discharges is collected. Phenomena such as the oscillation of the gas bubble and the thermal instability are further investigated. The results of an experiment performed to investigate the discharge instability under various conditions in a liquid dielectric will be discussed and compared with theoretical results. The main objective of the thesis is to establish the most important phenomena in discharges occurring in liquids.

CHAPTER 2

DYNAMICS OF THE STABLE DISCHARGE IN A LIQUID

2.1 Plasma channel created by a spark discharge in gases and liquids

The dynamics of a spark discharge in gas or liquid have been discussed by many authors (Skvortsov et al[3], Abramson et al[4,5], Drabkina[6], Gegechkori[7], Braginskii[8], Andreev et al[9,10], Egorova et al[11]). All authors assume a cylindrical shape for the radially expanding plasma column which is pushing a shock wave into the undisturbed environment. The expansion of a spark channel in a gaseous environment was first described by Drabkina et al[4,6] in 1945 and 1951.

According to Drabkina[3] the discharge energy is converted into the creation of a pressure disturbance with a shock on the edge of the disturbance. By using the hydrodynamic equation Drabkina[3] was able to solve for the distribution of the pressure, density and temperature behind the front edge of the expanding disturbance. The following equations describe the motion of the radius of the channel and the shock wave

$$r_s(t) = \left(\frac{\alpha}{\rho_o}\right)^{1/4} \left[\int_o^t \left(\frac{E(t)}{\ell}\right)^{1/2} dt\right]^{1/2} \qquad (2.1)$$

$$r_k(t) = L\left(\frac{\rho_N}{\rho_o}\right)^{p} \left(\frac{E(t)}{\ell}\right)^{M} \left[\int_o^t \left(\frac{E(t)}{\ell}\right)^{1/2} dt\right]^{N} \qquad (2.2)$$

where $r_s(t)$ - channel radius, $r_k(t)$ - shock wave radius, t - time, $E(t)$ - released energy up to time t, ℓ - length of the spark, ρ_N - gas density at 760 torr, ρ_o - gas density in the observed space,

α, L, p, M, N - constants depending on the gas properties.

The Drabkina theory has been discussed and experimentally verified by other authors[3,5,7]. In 1958 a more accurate theory was developed by Braginskii[8] which was later partially improved and completed. According to many authors, the Braginskii theory is in very good agreement with present experimental data.

In the Braginskii theory the plasma channel is assumed to be a homogeneous cylinder. The energy released in the spark is accounted for by an increase in the internal energy (dissociation, ionization, increased temperature) and by the expansion of the gas in the channel.

If the effects of radiation, skin-effect and magnetic forces are neglected and the electrical conductivity assumed approximately constant throughout the plasma column diameter, the quasi-self-similar solution for the cylindrical shock wave from the energy balance equation gives the following expression for the channel radius:

$$r_k(t) = \left[\frac{4}{\pi^2 \rho_o \xi \sigma} \right]^{1/6} \left[\int_o^t J^{2/3} dt \right]^{1/2} \tag{2.3}$$

where J - electric current, σ - electric conductivity, ρ - constant depending on the gas properties.

The Braginskii theory has been successfully used by many authors[9,10,11]. The best discussion and comparison between Drabkina's[6] experimental data and the Braginskii theory appears in the work of Koppitz[12] and Tholl[13]. Koppitz[12] has improved Braginskii's expression for the latter stages of the discharge where the initial assumptions are no longer fulfilled.

For the description of a spark discharge in a liquid both the Braginskii[8] and Drabkina[5] theories may be used. The difference between the case of a discharge in a gaseous medium and that of a discharge in a liquid is that in the case of a liquid the surrounding medium is less compressible and is more dense. As a result more energy is converted into the creation of the shock wave and into the kinetic energy of the moving liquid. Naturally the pressure inside such a discharge is considerably higher than in a similar discharge in a gaseous environment.

The cylindrical model will also be used to describe the spark discharge in a liquid (see fig. 2.1a). The assumed density and temperature profiles in the gas bubble are depicted in Figure (2.1b).

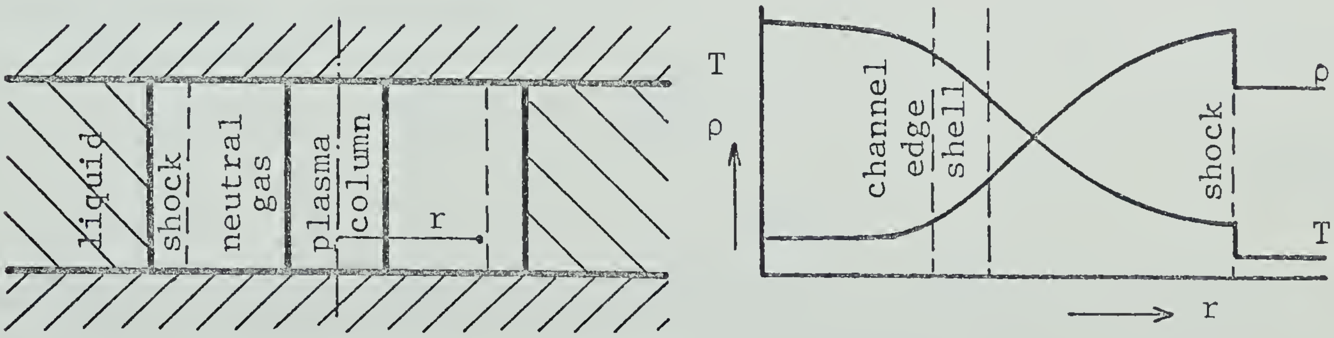

(a) (b)

Fig. (2.1) The cylindrical discharge model with temperature T and density ρ distribution

2.2 The steady plasma column of a discharge in a liquid

If liquid vaporization is neglected, the stable arc discharge in a liquid environment is similar to a discharge in a solid tube with a variable diameter. Such a discharge is described in many publications, the most important of which are by Hoyaux[1], Finklenburg[14,15] Maecker[16], Ecker and Zoller[17].

The high pressure, high current and the thermally inhomogeneous plasma column is described in detail by Ecker and Zoller[17].

Their theory does not require the Shotky assumption of a constant temperature across the plasma column. Their results provide the basis for the thermal instability described by Ecker, Kroll, Zoller[18]. The theory is based on a model consisting of a infinitely long cylindrical plasma column with insulated walls and a radius R. The plasma is taken as being weakly ionized across the column. The result of the analysis is the following system of two coupled differential equations which include all temperature effects:

$$\frac{1}{r}\frac{d}{dr}\left(rD[T]\frac{dn}{dr}\right) + \frac{1}{r}\frac{d}{dr}\left(rnD[T]\frac{d}{dr}\ln T\right) + \alpha[T]n = 0 \qquad (2.4)$$

$$\frac{1}{r}\frac{d}{dr}\left(r\lambda[T]\frac{dT}{dr}\right) + eE^2\mu_e[T]n = 0 \qquad (2.5)$$

with the boundary conditions

$$\begin{array}{lll} r = 0 & \frac{dn}{dr} = 0 & \frac{dT}{dr} = 0 \\ r = R & n = 0 & T = T_{wall} \end{array} \qquad (2.6)$$

where D - ambipolar diffusion coefficient, r - radius, λ - heat conductivity coefficient, T - neutral gas temperature, α - particle production coefficient, n - particle density, e - particle charge, E - longitudinal electric field, μ_e - electron mobility.

These equations reveal a similarity law. They are not analytically solvable and therefore a numerical solution is necessary. The similarity law is: In plasma columns with identical values of R_p and E/p the radial temperature distributions are identical and the density distributions similar. The density is directly and the current inversely proportional to the pressure.

A typical change of the radial neutral gas temperature and

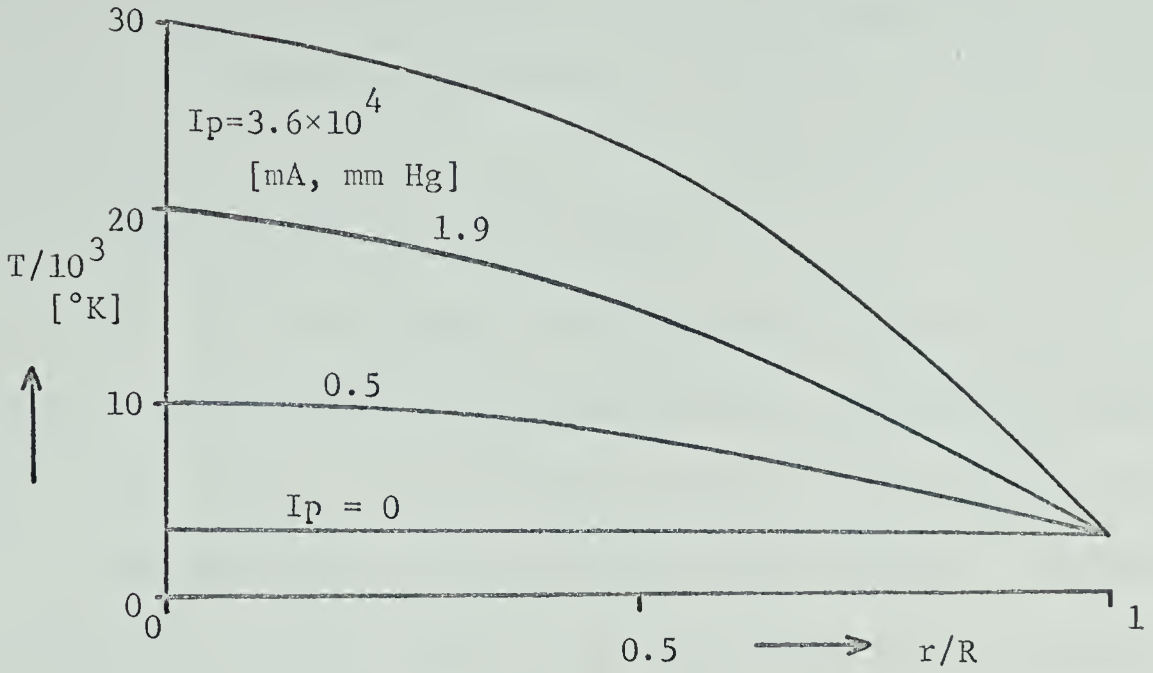

Fig. (2.2a) Typical change of the radial gas temperature distribution (after Ecker and Zoller[18])

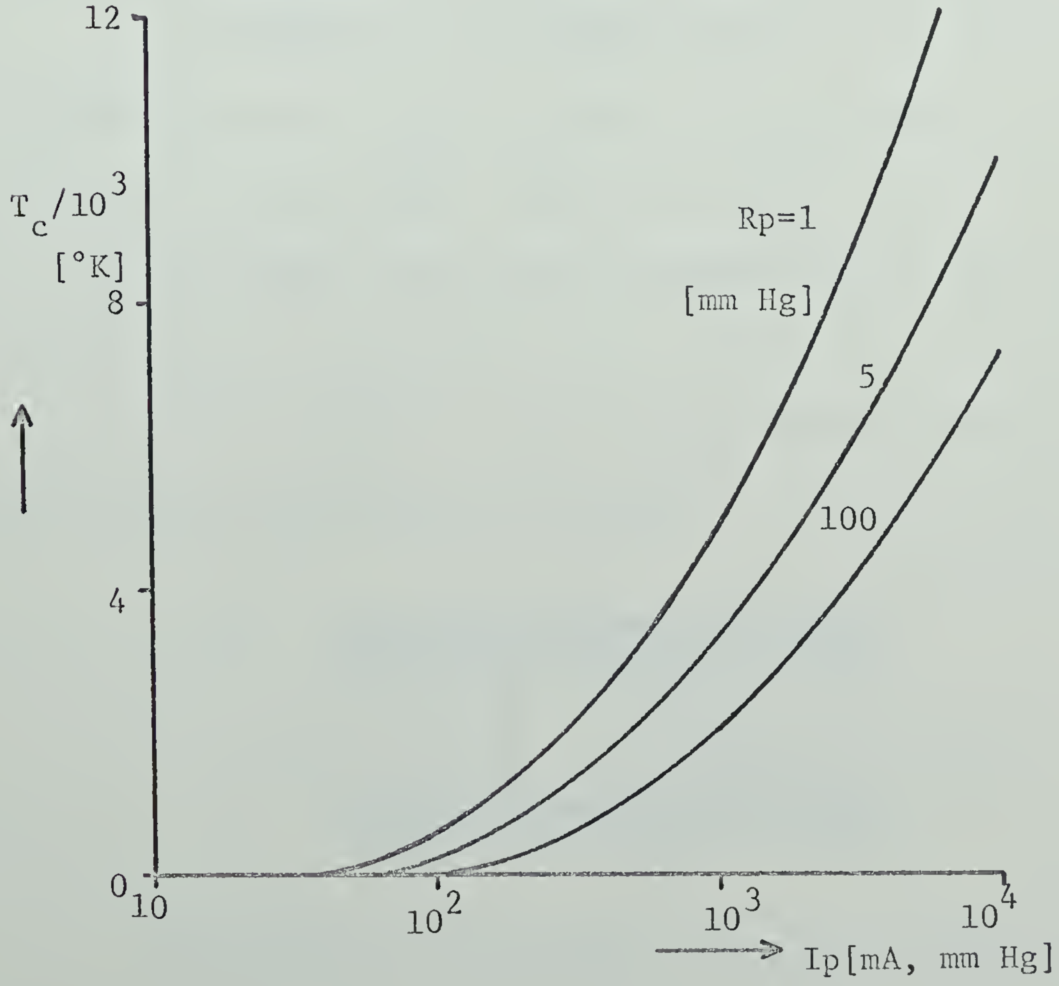

Fig. (2.2b) Dependence of the axial gas temperature T_c on pressure P, current I and radius R (after Ecker and Zoller[18])

the dependence of the axial neutral gas temperature for a helium column as calculated by Ecker and Zoller[18] are shown in Fig. 2.2a and 2.2b.

2.3 Oscillation of the gas bubble

For the further investigation of the processes in the spark gap, a description of the behaviour of a simple gas bubble in the gap area is useful. In particular, when the spark discharge extinguishes the remaining gasses build up just such a bubble. The behavious of the bubble is determined by the conditions which prevailed at the end of the discharge. In other words, the pressure, temperature, etc. which prevailed at the end of discharge can be deduced if a suitable record and description of the gas bubble is available.

The shape of the bubble depends on the shape of the electrodes. A cylindrical shape for the bubble will be assumed for the case of two parallel electrodes and a spherically shaped bubble for the case of two tip electrodes. The first approximation to the solution for the oscillation of a gas bubble will be obtained by considering the ideal case with no friction, no heat exchange between bubble and environment and a perfect gas inside the bubble.

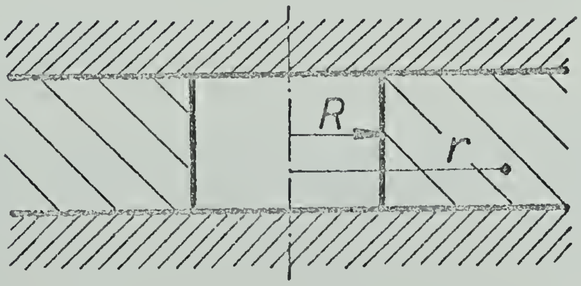

Fig. (2.3) The oscillating cylindrical bubble

The equation of motion for a cylindrical bubble in Fig. (2.3) can be derived from Bernoulli's equation as follows:

$$\frac{\partial\phi}{\partial t} + \frac{1}{2}\dot{r}^2 + \frac{P}{\rho} = f(t) ; \quad \dot{r} = \dot{R}\frac{R}{r} ; \quad \dot{r} = \frac{\partial\phi}{\partial r} \quad ; \quad \phi = \dot{R}R \ln r$$

where ϕ - velocity potencial, ρ - liquid density, $f(t)$ - arbitrary function of time, t - time.

$$\frac{P}{\rho} + \ln r \frac{\partial(\dot{R}R)}{\partial t} + \frac{1}{2}\dot{R}^2 \frac{R^2}{r^2} = f(t) \qquad \text{for } r \to \infty \quad f(t) = 0$$

$$\frac{P}{\rho} = -[\ln r \; (\ddot{R}R + \dot{R}^2) + \frac{1}{2}\dot{R}^2 \frac{R^2}{r^2}]$$

for $r = R$ we get

$$\frac{P}{\rho} = -[\ln R \; (\ddot{R}R + \dot{R}^2) + \frac{1}{2}\dot{R}^2]$$

but

$$\ddot{R} = \frac{d}{dR}(\frac{1}{2}\dot{R}^2) = \dot{R}\frac{d\dot{R}}{dt}\frac{dt}{dR}$$

$$\frac{P}{\rho} = -[(R\frac{1}{2}\frac{d\dot{R}^2}{dR} + \dot{R}^2) \ln R + \frac{1}{2}\dot{R}^2]$$

For an adiabatic compression and for $r \to \infty$; $p \to p^*$ we get

$$\frac{p_1}{p + p^*} = (\frac{R}{R_1})^{2\gamma}$$

where $p_1 = p^* + p(R_1)$

R_1 - minimal radius or initial radius

γ - specific heat ratio

then $p = p_1(\frac{R_1}{R})^{2\gamma} - p^*$

$$(R\frac{1}{2}\frac{d\dot{R}^2}{dR} + \dot{R}^2) \ln R + \frac{1}{2}\dot{R}^2 = \frac{p^*}{\rho} - \frac{p_1}{\rho}(\frac{R_1}{R})^{2\gamma}$$

$$(R^2\frac{d\dot{R}^2}{dR} + 2\dot{R}^2R) \ln R + R\dot{R}^2 = \frac{2}{\rho} \quad (p^*R - p_1\frac{R_1^{2\gamma}}{R^{2\gamma-1}})$$

but $$\frac{d}{dR}(R^2\dot{R}^2 \ln R) = (2R\dot{R}^2 + R^2\frac{d\dot{R}^2}{dR}) \ln R + R\dot{R}^2$$

Substituting we get

$$R^2\dot{R}^2 \ln R = \int_{R_1}^{R} \frac{2}{\rho}\ [p^*R - p_1 \frac{R_1^{2\gamma}}{R^{2\gamma-1}}]\quad dR =$$

$$= \frac{2}{\rho}\ [\frac{p^*}{2}(R^2 - R_1^2) - \frac{p_1 R_1^{2\gamma}}{2-2\gamma}(R^{2-2\gamma} - R_1^{2-2\gamma})]$$

$$t = \int_{R_1}^{R} \frac{\sqrt{\ln R}\quad dR}{\sqrt{\frac{1}{\rho}\left[\frac{p_1}{\gamma-1}\left\{\left(\frac{R_1}{R}\right)^{2\gamma} - \left(\frac{R_1}{R}\right)^2\right\} + p^*\left\{1 - \left(\frac{R_1}{R}\right)^2\right\}\right]}}$$

$$t = \sqrt{\frac{\rho}{p^*}} \int_{R_1}^{R} \frac{\sqrt{\ln R}\quad dR}{\sqrt{\frac{p_1}{p^*(\gamma-1)}\left[\left(\frac{R_1}{R}\right)^{2\gamma} - \left(\frac{R_1}{R}\right)^2\right] + 1 - \left(\frac{R_1}{R}\right)^2}} \tag{2.7}$$

For $R = R_{max} = R_3$ $\qquad \frac{dR}{dt} = 0$

Then
$$p_1 = \frac{p^*\left[1 - \left(\frac{R_1}{R_3}\right)^2\right]}{\left(\frac{R_1}{R_3}\right)^{2\gamma} - \left(\frac{R_1}{R_3}\right)^2}\ (\gamma - 1) \tag{2.8}$$

Similarly we get for the spherical bubble

$$t = \sqrt{\frac{3}{2}\rho} \int_{R_1}^{R} \frac{dR}{\sqrt{\frac{p_1}{\gamma-1}\left[\left(\frac{R_1}{R}\right)^3 - \left(\frac{R_1}{R}\right)^{3\gamma}\right] - p^*\left[1 - \left(\frac{R_1}{R}\right)^3\right]}} \tag{2.9}$$

and
$$p_1 = \frac{p^*\left[1 - \left(\frac{R_1}{R_3}\right)\right]^3}{\left(\frac{R_1}{R_3}\right)^3 - \left(\frac{R_1}{R_3}\right)^{3\gamma}}\ (\gamma - 1) \tag{2.10}$$

In either of the two expressions for t, the integrals that appear must be evaluated numerically. If the initial pressure $p_1 \neq p^*$, the above equations give the result that the bubble will be able to oscillate for an infinitely long time. This is of course not true in practice since the oscillation will be damped through viscous losses in the liquid. For a cylindrical bubble in water with $\gamma = 1.4$, $R_1 = 1$ mm and $R_2 = 10$ mm we get $p_1 = 48.6$ atm. and $p_3 = 0.075$ atm. The graph of function R(t) for the first half wave is shown in Fig. (2.4). The equation of motion for a spherical bubble may be also written in dimensionless form. The dependance of $\frac{R}{R_1}$ on $t/ (\frac{3}{2} \rho R_1)$for different values of γ and $p_1 = 50$ atm. is shown in Figure (2.5).

Therefore, just the value of the repetition frequency (which can be easily measured, e.g. piesoelectric probe) is insufficient for the calculation of the pressure p. That is why an optical record is necessary.

A comparison between calculated values and values obtained from an optical record for a spherical bubble in petroleum after a 0.1 joule discharge 100 μsec long is given in Figure (2.6) where $p_1 = 40$ atm and $p_3 = 0.085$ atm. The difference between the measured and calculated values is the result of energy losses such as heat exchange, friction, vaporization etc. Each energy loss increases R_1 and decreases R_3. This causes the change in the time scale in Figure (2.5). Also any deviation from the assumed spherical shape will result in a difference between the measured and calculated values.

A nomogram has been computed for the case of a spherical bubble (Fig. (2.7)) from which values of p_1 may be directly read for

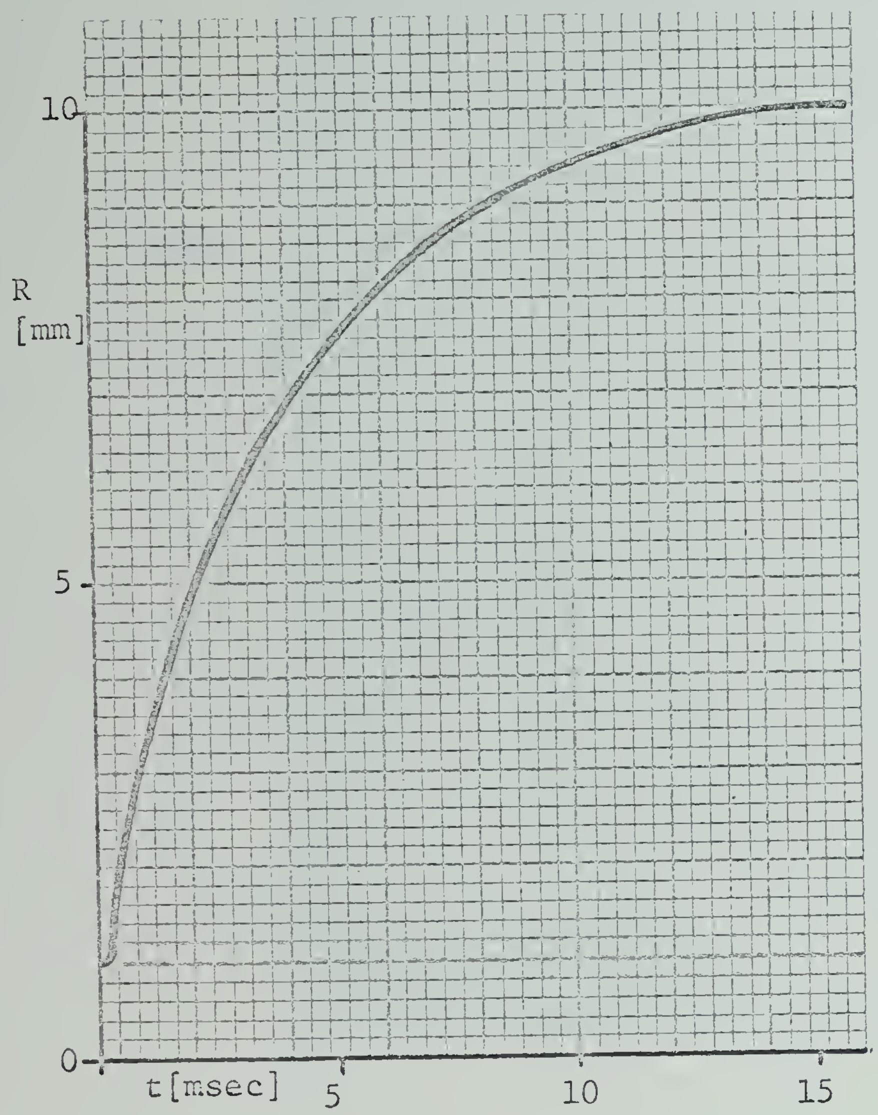

Fig. (2.4) The dependence of radius R on time t for an oscillating cylindrical bubble in water ($\gamma = 1.4$)

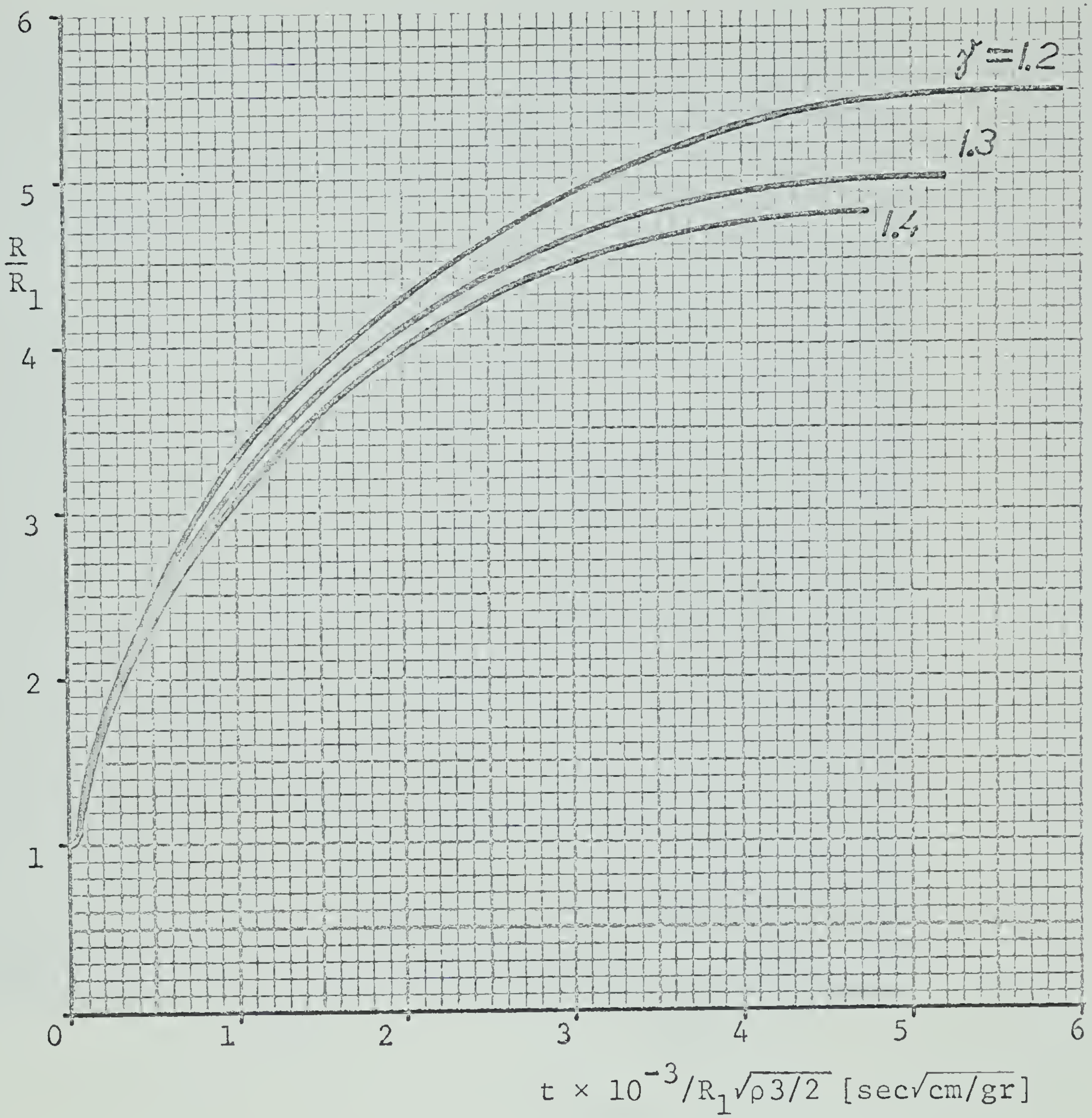

Fig. (2.5) The dependence of R/R_1 on $t/\sqrt{3/2}\,\rho R$ for a spherical bubble in water/

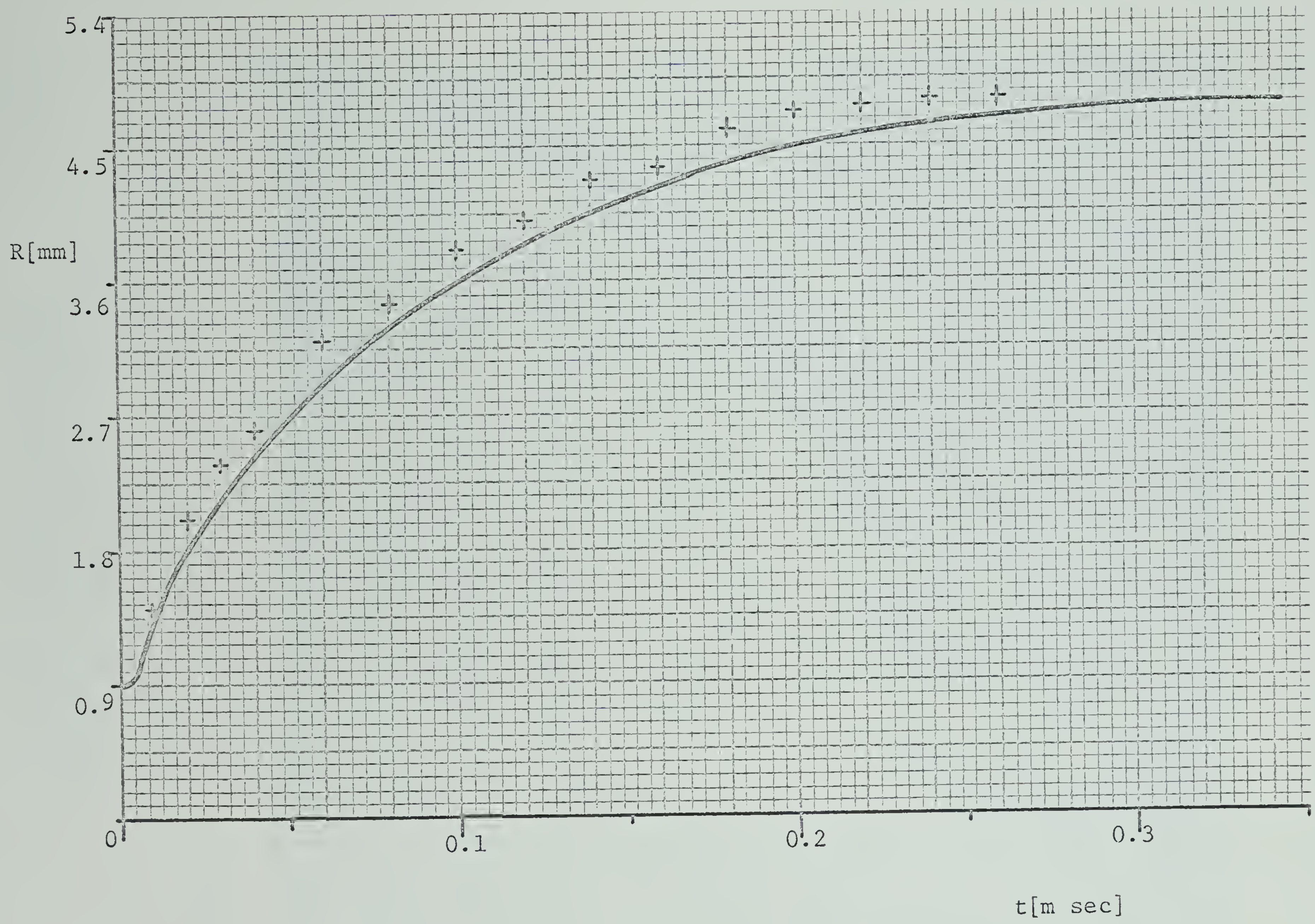

Fig. (2.6) The measured (+) and calculated (——) values of radius R of an oscillating cylindrical bubble in water.

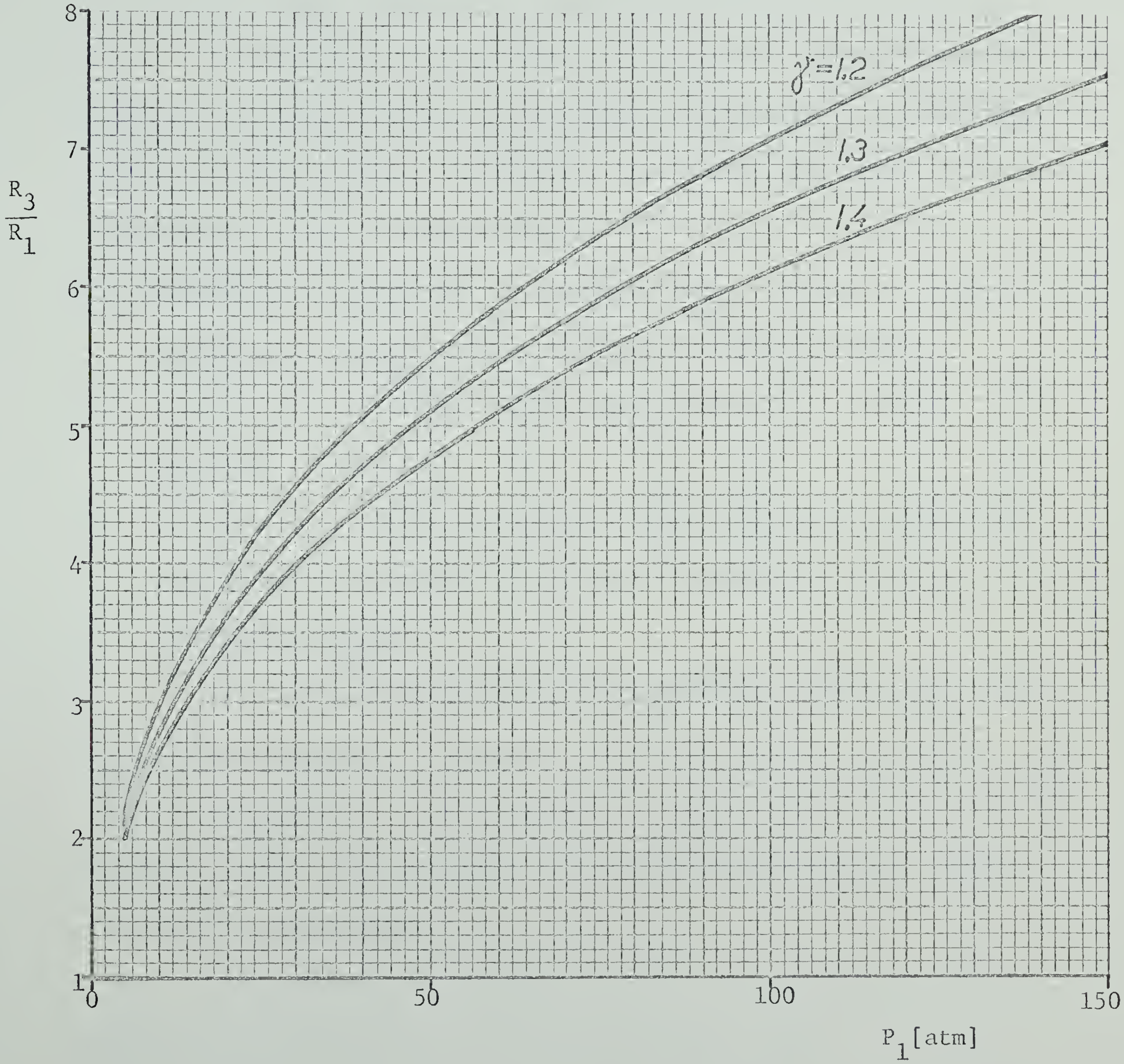

Fig. (2.7) The dependence of R_3/R_1 on pressure p_1 for a spherical bubble in water for various values of γ.

different ratios of R_3/R_4 and different values for γ assuming $p^* = 1$ atm. This may be used to obtain a quick overall picture by evaluating the bubble oscillation records.

2.4 The frictional losses of a cylindrical bubble oscillation

The viscous properties of the liquid are also an important factor in the investigation of the dynamic processes of a discharge between two flat parallel electrodes. The frictional losses could be responsible for all of these effects:

(1) damping of oscillations of a simple bubble through the transformation of liquid kinetic energy into thermal energy,

(2) reduction of the shock wave strength, especially near the electrode surface,

(3) increased pressure in the plasma channel during its expansion because of the increase in the force required to move the surrounding liquid.

The exact description of the behaviour of the viscid fluid around the expanding or collapsing discharge channel is a rather complicated problem. In this chapter an approximate solution will be obtained, which could give some idea of the significance of liquid viscosity in our problem.

The cylindrical approximation for the oscillating bubble holds well in the middle part of the discharge column. Near the electrodes this approximation is probably inaccurate even in case when liquid viscosity is ignored. The theory of viscous flow gives the frictional losses to be greatest near the edge of the gas cylinder, where, if the Reynold's number is sufficiently large, the flow is laminar with the appropriate boundary layer with a shear type of flow.

In this case the faster the flow, the thinner is the boundary layer and the larger are the friction losses per unit area. The thickness of the boundary layer in such a case rises with increasing distance from the middle of the cylinder. For distances from the middle of the cylinder which are larger than the distance r* in which the boundary larger thickness is equal to the half of the distance between electrodes, the flow is no longer "laminar with a boundary layer" but instead "laminar viscous flow with small Reynolds number" (Fig. (2.8)).

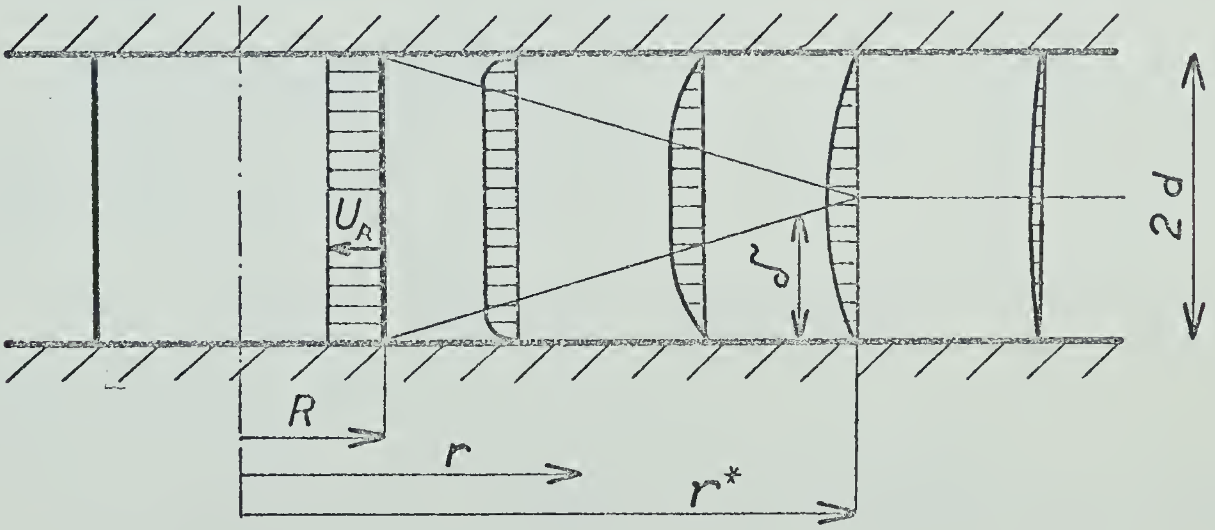

Fig. (2.8) The viscous flow around the oscillating cylindrical bubble

The problem will be solved separately for

(a) r > r* - case of radial laminar viscous flow between two plates with a small Reynolds number".

(b) r < r* - case of the radial viscous flow with a boundary layer.

The following well known formula describes the uniform Laminar viscous flow with a small Reynolds number between two plates:

$$U(y) = \frac{c}{2\mu}(d^2 - y^2)$$

where 2d - distance between plates

μ - viscosity

y - coordinate perpendicular to plates

c - constant proportional to the fluid velocity

The average velocity

$$\overline{U} = \frac{1}{2d} \int_{-d}^{d} U dy = \frac{2}{3} U_{max} \quad ; \quad U_{max} = \frac{cd^2}{2\mu}$$

For the cylindrically symmetric case, in Fig. (2.8),

$$U(r) = U_R \frac{R}{r}$$

$$U_{max} = \frac{3}{2} U_R \frac{R}{r} \tag{2.11}$$

$$c = \frac{2\mu}{d^2} U_{max} = 3U_R \frac{R}{r} \frac{\mu}{d^2}$$

The viscous shearing stress tensor

$$\tau_o = \mu \left(\frac{\partial u}{\partial y}\right)_{y=d} = \mu \left(\frac{2cy}{2\mu}\right)_{y=d} = cd = 3U_R \frac{R}{r} \frac{\mu}{d}$$

The total frictional force for r > r*

$$F_a = 2 \int_{r^*}^{r} 2\pi r \tau_o dr = \frac{12U_R \pi R \mu}{d} \int_{r^*}^{r} dr = \frac{12U_R R \pi \mu}{d} (r-r^*) \tag{2.12}$$

so for $r \to \infty$ $\qquad F_a \to \infty$

For case (b) where r < r* we will use the boundary layer theory. The direct calculation through the evaluation of the boundary layer thickness is not convenience because it leads to an infinite value for τ_o in the case where the boundary layer thickness δ is equal to zero i.e. for r = R. A more suitable method is the Karman-Pohlhausen's momentum integral technique which allows the elimination of the boundary layer thickness before integration. This method is adapted below for the case of radial flow.

From Euler's momentum theorem

$$\sum F_r = \int_S \rho u q \cos\gamma \, ds \qquad F_r || u; \; q^2 = u^2 + v^2 + w^2$$

where ΣF_r - the sum of the external forces acting on the fluid in the considered volume q - the velocity vector, u, v, w, -components of vector q.

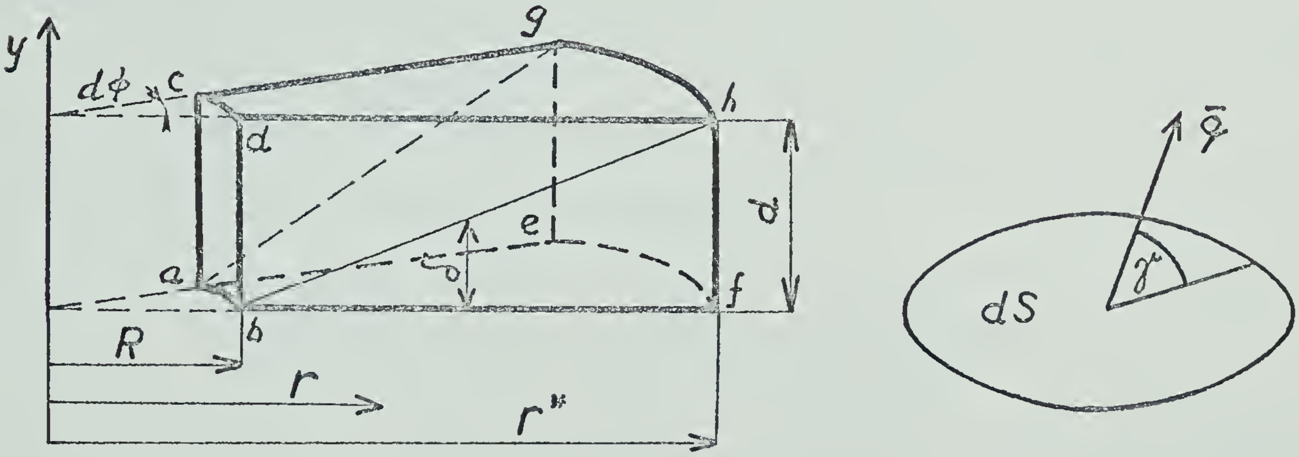

Fig. (2.9) The segment of the moving anulus and its surface element

The forces acting on the segment of the anulus in Figure (2.9) will now be examined.

The flow through walls

$$\left.\begin{array}{ll} abef = 0 & \text{(rigid wall)} \\ cdgh = 0 & \text{(because of symmetry)} \\ \left.\begin{array}{l} bdhg = 0 \\ aceg = 0 \end{array}\right\} & \text{(radial flow)} \end{array}\right\} \quad g \cos\gamma = 0$$

The total radial force acting on the cylinder

$$F_b = 2\Big(\underbrace{\int_0^{2\pi} F_{abcd} \, d\phi}_{I_1} + \underbrace{\int_0^{2\pi} F_{efgh} \, d\phi}_{I_2} \Big)$$

The factor of 2 accounts for the bottom and top parts of the cylinder.

$$I_1 = 2\pi R \int_0^d \rho u g \cos \gamma \, dy = \rho U_R^2 \, 2\pi R d$$

since $u(y) = U_R$ = constant at the interface between the expanding bubble and the liquid.

Now we assume the velocity distribution in the boundary layer to be

$$\frac{u}{U_{max}} = \sin\left(\frac{\pi}{2}\frac{y}{\delta}\right)$$

then similarly as in the previous case

$$\bar{u} = \frac{1}{2d}\left[2U_{max}(d-\delta) + 2\int_0^\delta U_{max} \sin\left(\frac{\pi}{2}\frac{y}{\delta}\right) dy\right]$$

Where the first term in the brackets contains the velocity profile in the area between the boundary layers and the second contains the velocity profile within the boundary layer

$$\bar{u} = \frac{1}{2d}\left[2U_{max}\left\{d + \delta\left(\frac{2}{\pi} - 1\right)\right\}\right] = U_{max}\left[1 + \frac{\delta}{d}\left(\frac{2}{\pi} - 1\right)\right]$$

also $\bar{u} = \frac{U_R R}{r}$ from the continuity equation.

Thus

$$U_{max} = \frac{U_R R}{r\left[1 + \frac{\delta}{d}\left(\frac{2}{\pi} - 1\right)\right]} \tag{2.13}$$

and for $r = r^*$ $\delta = d$ so that

$$U_{max_{r=r^*}} = \frac{U_R R}{r^* \frac{2}{\pi}} = \frac{\pi}{2}\frac{U_R R}{r^*} = 1.57 \frac{U_R R}{r^*}$$

Equation (2.11) gives

$$U_{max_{r=r^*}} = 1.5 \frac{U_R R}{r^*}$$

The difference in the values for $U_{max_{r=r^*}}$ is caused by the assumption of a different kind of velocity distribution approximation in the boundary layer.

Then

$$I_2 = 2\pi r^* \int_o^d \rho U^2_{max_{r=r^*}} \sin^2\left(\frac{\pi}{2}\frac{y}{d}\right) dy = \pi r^* \rho U_{max_{r=r^*}} d =$$

$$= \left(\frac{\pi}{2}\frac{U_R R}{r^*}\right)^2 \pi r^* \rho d = \frac{\pi^3 U_R^2 R^2 \rho d}{4r^*}$$

$$F_b = 4\pi R U_R^2 \rho d \left[\frac{\pi^2 R}{8r^*} - 1\right]$$

The radius r* is dependent on the viscosity and the velocity U_R (the smaller the value of r* the larger is μ and the smaller is U_R).

The value of r* will now be calculated. Because $r \to r^*$ if $\delta = d$, the shape of the boundary layer is required. As in the case of a uniform flow past a flat plate[19], the following approximation is made for δ.

$$\delta = 5\sqrt{\frac{\mu(r-R)}{\rho\ U_{max}}}$$

Then from equation (2.13)

$$U_{max}(r) = \frac{U_R R}{r\left[1 + \dfrac{5(\frac{2}{\pi} - 1)}{d}\sqrt{\dfrac{\mu}{\rho}\dfrac{(r-R)}{U_{max}}}\ \right]}$$

or

$$U_{max} + \sqrt{U_{max}}\ a = b \qquad \text{where}$$

$$a = \frac{5(\frac{2}{\pi} - 1)}{d}\sqrt{\frac{\mu}{\rho}(r-R)} \quad ; \qquad b = \frac{U_R R}{r}$$

The square of the above equation gives

$$U^2_{max} - (2b + a^2)\ U_{max} + b^2 = 0 \tag{2.14}$$

Equation (2.14) also corresponds to the equation

$$U_{max} - \sqrt{U_{max}} \; a = b$$

but for $b \geq 0$; $a \leq 0$ and $U_{max} \geq 0$

the required solution is

$$U_{max} = b + \frac{a^2}{2} + \sqrt{a^2 b + \frac{a^2}{4}}$$

By substituting for a and b

$$U_{max} = \frac{U_R R}{r} + \frac{1}{2} \frac{25\mu(r-R)(\frac{2}{\pi}-1)^2}{d^2\rho} + \sqrt{\frac{25\mu(r-R)(\frac{2}{\pi}-1)^2}{d^2\rho}\left[\frac{U_R R}{r} + \frac{1}{4}\frac{25\mu(r-R)(\frac{2}{\pi}-1)^2}{d^2\rho}\right]}$$

But case (a) (laminar flow) gives

$$U_{max} = \frac{U_R R}{r^*} \frac{\pi}{2} \qquad \text{at } r = r^*$$

By substituting this condition into the previous equation we finally get

$$\frac{U_R R}{r^*}(\frac{\pi}{2} - 1) = \frac{1}{2} \frac{25\mu(r^*-R)(\frac{2}{\pi}-1)^2}{d^2\rho} + \sqrt{\frac{25\mu(r^*-R)(\frac{2}{\pi}-1)^2}{d^2\rho}\left[\frac{U_R R}{r^*} + \frac{1}{4}\frac{25\mu(r^*-R)(\frac{2}{\pi}-1)^2}{d^2\rho}\right.} \tag{2.15}$$

From the above equation a value for r* may be obtained through the use of a numerical iteration method. The force $F = F_a + F_b$ represents the total radial frictional force which acts on the cylinder of radius R, and length 2d expanding or contracting radially with velocity U_R. The integral denoted by F_a diverges as $r \to \infty$. However, because of the slight compressibility in the liquid, deformations and finite dimensions of the electrodes the force F_a is in fact finite. To get a reasonable estimate of the friction force, the integration will be performed for $r \leq r_{max}$ only, where $r_{max} = 1 \div 10$ cm. For a typical case R = 0.1 cm, 2d = 0.1 cm, $U_R = 5{,}000$ cm/sec, $\mu_{H_2O} = 0.003 \text{ cm}^2/\text{sec}$. and T = 100°C. Thus the Reynold's number is

$$R = \frac{U_R d\rho}{\mu} = \frac{5{,}000 \times 0.05}{0.003} = 83{,}300$$

The viscous energy losses during a half period of oscillation will be calculated numerically under the following assumptions.

(1) the total amount of viscous losses during a half period is much smaller than is the amount of mechanical energy stored in oscillation bubble. Under this assumption the shape of the oscillation bubble does not change appreciably and therefore calculations will be made with values U_R, t, T holding for inviscid oscillations.

(2) friction losses will be calculated for small time intervals assuming that during this interval U_R, t, T are constant.

The viscous losses of an oscillating cylindrical bubble whose radial time dependence is given in Figure (2.5) have been calculated numerically for water and silicon oil. The application of the Newton-Raphson method for the solution of r* in equation (2.15) gives

$$r^*_{i+1} = r_i{}^* - \frac{1.65A(r_i{}^*-R) + 0.57\,\frac{U_R R}{r_i{}^{*2}} + 1.81B}{1.65A + 0.57\,\frac{U_R R}{r_i{}^{*2}} + \frac{1.81}{2B}\left[1.65A^2(r^*-R) + \frac{AR^2U_R}{r^{*2}}\right]}$$

where $A = \dfrac{\mu}{d^2\rho}$

$$B = \sqrt{A(r^*-R)\left[\frac{U_R R}{r^*} + 0.825A\,(r^*-R)\right]}$$

The dependence of $R_1 r^*$ and w on t is shown in Figure (2.10) for the case where water and cylindrical electrodes with a diameter of 10 cm are used. w represents the total frictional loss up to time t, that is

$$w = \int_{R_1}^{R} (F_a + F_b)\, dR \qquad \text{where } R = R(t)$$

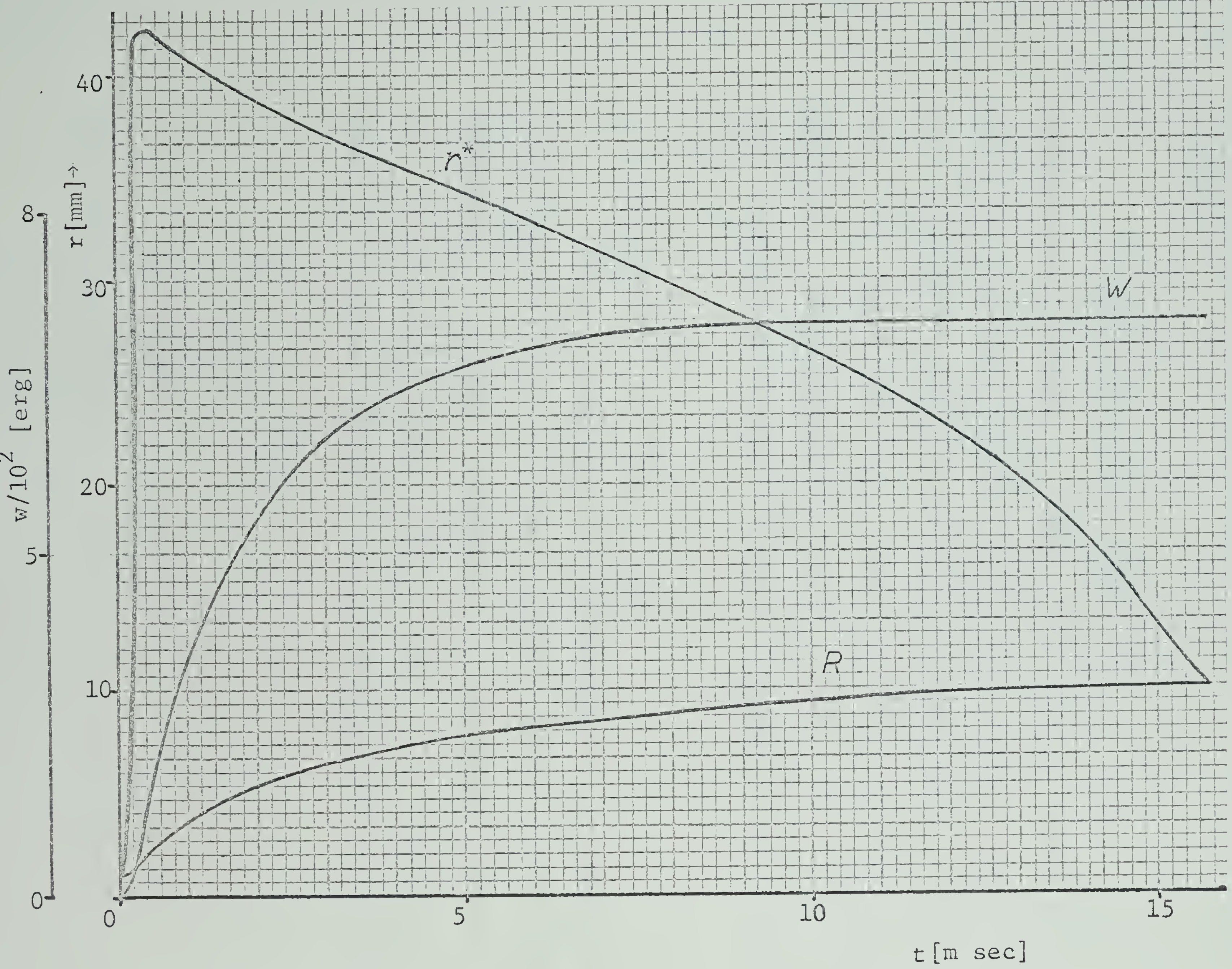

Fig. (2.10) The dependence of radii R and r*, and frictional losses w for an oscillating cylindrical bubble in water.

The total energy of the oscillating bubble w_T is equal to half of that which is done by an adiabatic expansion of the bubble from a diameter R_1 to R_3.

$$w_T = \frac{1}{2} \frac{1}{\gamma-1} (p_3R_3^2 - p_1R_1^2)\ 2\pi d$$

For the case considered in Figure (2.10) with 2d = 1mm, $w_T = 1.05 \times 10^3$ dyn cm the frictional losses during a half period of oscillation for water and silicon oil (μ = 1.7 g/sec cm) are 8.28×10^2 ergs and 2.93×10^4 ergs respectively. Thus the initial assumptions are invalid because the energy losses are too large. Therefore the frictional forces must be considered through the numerical integration of the equation (2.7).

2.5 Dissociation of the water vapors

For many important investigations, for instance of diffusion, thermal conductivity etc., the composition of the gasses contained in the bubble is required. In this section the simple case of dissociation of water vapours will be investigated. For simplicity only three simple dissociation reactions (no ionization) will be considered

$$H_2O \rightleftarrows H_2 + \frac{1}{2} O_2$$

$$H_2 \rightleftarrows 2H$$

$$O_2 \rightleftarrows 2O$$

Other reactions such as

$$OH \rightleftarrows \frac{1}{2} O_2 + \frac{1}{2} H_2$$

$$O_3 \rightleftarrows \frac{3}{2} O_2$$

will be neglected.

The calculation of the degree of reaction ε is well described in the literature[29]. The equilibrium state for the reaction

$$aA + bB \rightleftarrows cC + dD$$

is described by the law of mass action:

$$\frac{X_C^{\ c}\ X_D^{\ d}}{X_A^{\ a}\ X_B^{\ b}}\ P^{c+d-a-b} = K$$

where the X's are mole fractions (functions of ε)

a,b,c,d - stoichiometric coefficients

P - pressure

K - the equilibrium constant

Values of K are tabulated in some publications for various temperatures and pressures. Unfortunately this information is not complete and it is necessary to resort to extrapolation. However, some of this data is tabulated for the inverse reactions. In such cases, values of K for the normal type of reaction may be calculated. That is, if K relates to the reaction

$$aA + bB \rightleftarrows cC + dD$$

and if $\bar{K}$ corresponds to the reaction

$$cC + dD \rightleftarrows aA + bB$$

the formal relationship between K and $\bar{K}$ is as follows:

$$K = f(\varepsilon) \qquad \bar{K} = \frac{1}{f(1-\varepsilon)}$$

If $f(\varepsilon)$ and $\bar{K}$ are known; the value of K may be easily calculated.

For the reaction

$$H_2O \rightleftarrows H_2 + \frac{1}{2}\,O_2$$

the form of the law of mass action is as follows

$$\frac{\varepsilon^{3/2}}{(2+\varepsilon)^{1/2}(1-\varepsilon)}\ P^{1/2} = K$$

or

$$\frac{\varepsilon(3-\varepsilon)^{1/2}}{(1-\varepsilon)^{3/2}} \; \frac{1}{P^{1/2}} = \bar{K}$$

The Newton-Raphson method will be used for calculation of values for ε from the above equations on a computer

$$x_{i+1} = x_i - \frac{F(X_i)}{F'(X_i)}$$

If a value for $\bar{K}$ is available for water, then the use of the iteration formula gives

$$\varepsilon_{i+1} = \varepsilon_i + \sqrt{P}\,[\bar{K} - \varepsilon\sqrt{\frac{3-\varepsilon}{(1-\varepsilon)^3 P}}\,]\sqrt{(1-\varepsilon)^5(3-\varepsilon)}$$

If the value of K is available, the iteration formula gives

$$\varepsilon_{i+1} = \varepsilon_i + [K - \frac{\varepsilon^{3/2}}{(2+\varepsilon)^{1/2}(1-\varepsilon)} \; P^{1/2}\,]\,\frac{(2+\varepsilon)^{3/2}(1-\varepsilon)^2}{\varepsilon^{1/2}[3+\ (1-\varepsilon)]P^{1/2}}$$

Because the graph of $\log_{10}$ K against 1/T (Figure (2.11)) is approximately a straight line, K may be expressed as function of T as follows

$$\log_{10} K = a_1 \frac{1}{T} + b_1$$

where a_1 and b_1 are constants and T is in °K or

$$K = \exp\,[2.30261 \times (\frac{a_1}{T} + b_1)]$$

When P = 1 atmosphere, Figure (2.11) gives

$$a_1 = -13.1 \times 10^3 \qquad b_1 = +3.03$$

Similarly for the reaction

$$\frac{1}{2}O_2 \rightleftarrows 2O_2 \qquad a_2 = 12.8 \times 10^3 \qquad b_2 = 2.1$$

$$K_2 = \frac{2\varepsilon}{\sqrt{1-\varepsilon^2}} \; P^{1/2} \qquad K_2' = \frac{2}{\sqrt{(1-\varepsilon^2)^3}} \; P^{1/2}$$

$$\varepsilon_{i+1} = \varepsilon_i + \frac{1}{2}\left(K_2 - \frac{2\varepsilon}{\sqrt{1-\varepsilon^2}}\, P^{1/2}\right) \sqrt{\frac{(1-\varepsilon^2)^3}{P}}$$

and for the reaction

$$H_2 \rightleftarrows 2H \qquad a_3 = -23.48 \times 10^3 \qquad b_3 = 6.35$$

$$K_3 = \frac{4\varepsilon^2 P}{1-\varepsilon^2} \qquad K_3' = \frac{8\varepsilon}{(1-\varepsilon^2)^2}$$

$$\varepsilon_{i+1} = \varepsilon_i + \left(K_3 - \frac{4\varepsilon^2 P}{1-\varepsilon^2}\right) \frac{(1-\varepsilon^2)^2}{8\varepsilon}$$

From the above relations, values for ε_{H_2O}, ε_{H_2}, $\varepsilon_{O_2/2}$ may be calculated for particular values of the temperature T and the pressure P. Finally, the complete reaction is described by the following equation,

$$n_1H_2O \rightarrow n_2H_2O + n_3H_2 + n_4H + n_5O_2 + n_6O \qquad (2.15)$$

The reaction described by equation (2.15) is depicted graphically below

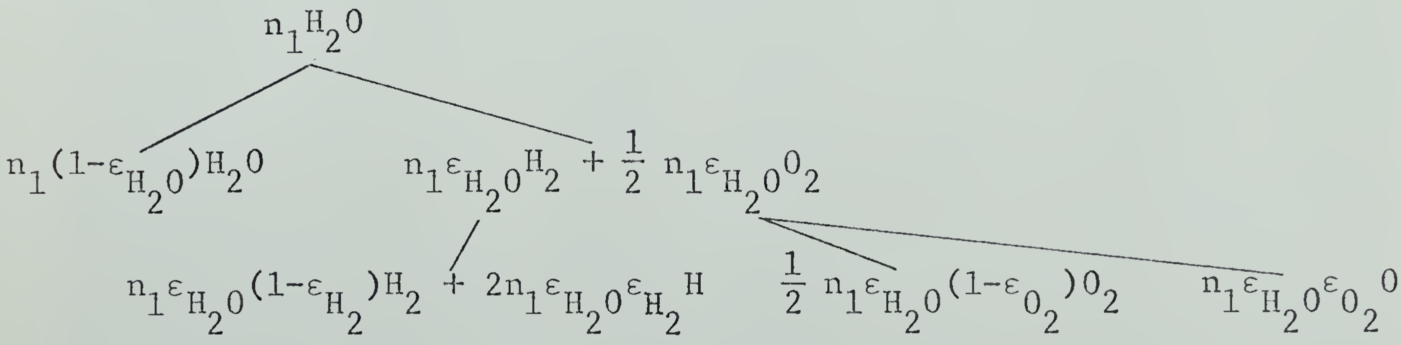
n_1H_2O
$n_1(1-\varepsilon_{H_2O})H_2O$
$n_1\varepsilon_{H_2O}H_2 + \frac{1}{2}\, n_1\varepsilon_{H_2O}O_2$
$n_1\varepsilon_{H_2O}(1-\varepsilon_{H_2})H_2 + 2n_1\varepsilon_{H_2O}\varepsilon_{H_2}H$
$\frac{1}{2}\, n_1\varepsilon_{H_2O}(1-\varepsilon_{O_2})O_2$
$n_1\varepsilon_{H_2O}\varepsilon_{O_2}O$

The dependance of the equilibrium constant ε on the temperature for the three basic reactions, with P = 1 atm., is shown in the Figure (2.12).

2.6 Ionization and thermal conductivity of the water vapours

The method for calculating the degree of ionization as well as the thermal conductivity of the water vapours is described in detail by Gross *et al.*[20]. For a complicated mixture of different kinds of molecules, atoms, ions and electrons, Gross *et al.*[20] derive from the system of Saha's equations and equations of state (under

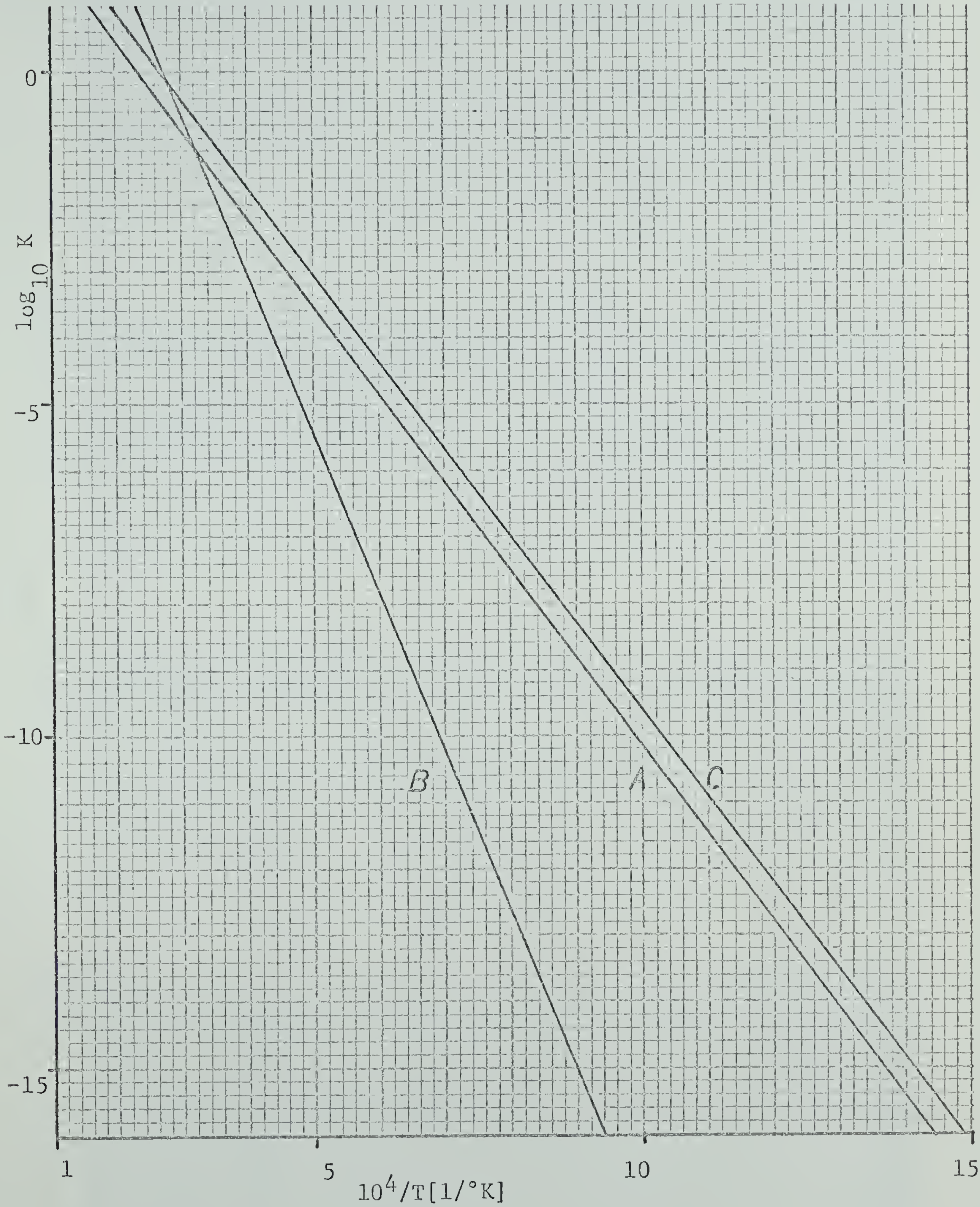

Fig. (2.11) The dependence of $\log_{10}K$ on 1/T for reactions

(A) $H_2O \rightleftarrows H_2 + O_2/2$

(B) $H_2 \rightleftarrows 2H$

(C) $O_2/2 \rightleftarrows O$

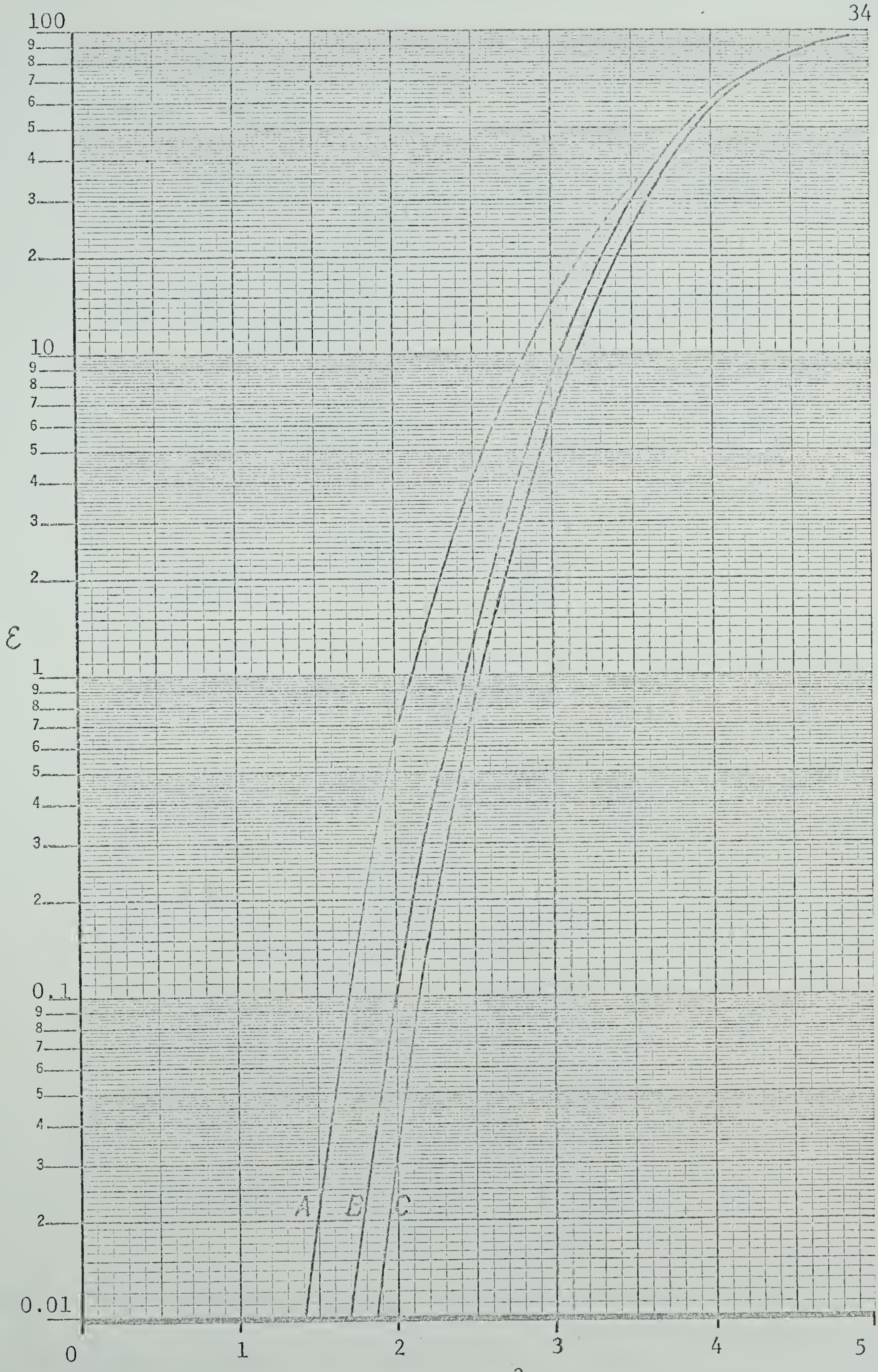

Fig. (2.12) The dependence of equilibrium constant ε on temperature T for the reactions (A) $H_2O \rightleftarrows H_2 + O_2/2$ (B) $H_2 \rightleftarrows aH$ (C) $O_2/2 \rightleftarrows O$ at 1 atmosphere pressure.

some simplificating assumptions) the following expressions for the particle concentrations:

$$n_e = \frac{S_H(T)}{kT}\left[\sqrt{1 + \frac{P}{S_H(T)}} - 1\right] \qquad \text{for } T < 2 \times 10^4\,{}^\circ K$$

$$n_e = \frac{P}{2kT}\,\frac{3+8\,\frac{S_{o^+}(T)}{P}}{3+7\,\frac{S_{o^+}(T)}{P}} \qquad \text{for } T > 2 \times 10^4\,{}^\circ K$$

$$n_e = \frac{P}{kT}\,\frac{4+9\,\frac{S_{o^{++}}(T)}{P}}{1+2\,\frac{S_{o^{++}}(T)}{P}} \qquad \text{for } T > 4.5 \times 10^4\,{}^\circ K$$

$$n_H = \frac{2}{3}\,\frac{P}{kT}\left[1 - \frac{2S_H(T)}{P}\left(\sqrt{1 + \frac{P}{S_H(T)}} - 1\right)\right]$$

$$n_{H^+} = \frac{2}{3}\,\frac{1}{kT}\,S_H(T)\left[\sqrt{1 + \frac{P}{S_H(T)}} - 1\right]$$

$$n_o = \frac{P}{3kT}\left[1 - 2\frac{S_o(T)}{P}\left\{\sqrt{1 + \frac{P}{S_o(T)}} - 1\right\}\right]$$

$$n_{o^+} = \frac{P}{3kT}\,\frac{3+8\,\frac{S_{o^+}(T)}{P}}{18+90\,\frac{S_{o^+}(T)}{P} + 98\left(\frac{S_{o^+}(T)}{P}\right)^2}$$

$$n_{o^{++}} = \frac{P}{3kT}\,\frac{6\,\frac{S_{o^+}(T)}{P} + 14\left(\frac{S_{o^+}(T)}{P}\right)^2}{18+90\,\frac{S_{o^+}(T)}{P} + 98\left(\frac{S_{o^+}(T)}{P}\right)^2}$$

$$n_{o^{+++}} = \frac{P}{3kT}\,\frac{3\,\frac{S_{o^{++}}(T)}{P} + 5\left(\frac{S_{o^{++}}(T)}{P}\right)^2}{4+16\,\frac{S_{o^{++}}(T)}{P} + 14\left(\frac{S_{o^{++}}(T)}{P}\right)^2}$$

where P - pressure; n_e, n_H, n_{H^+}, n_o, n_{o^+}, $n_{o^{++}}$, $n_{o^{+++}}$ - concentrations of electrons, hydrogen and oxygen atoms and ions respectively; S_H, S_{o^+}, and $S_{o^{++}}$ - right hand sides of the Saha equations, which have the general form

$$\frac{n_{i+1}}{n_i} p_e = \frac{2Z_{i+1}}{Z_i} \frac{(2\pi m_e)^{3/2}}{h} (kT)^{5/2} e^{-\frac{\varepsilon_i}{kT}}$$

where n_i, n_{i+1} - concentrations of particles in the i'th and i+1'th degree of ionization; Z_i, Z_{i+1} - partition functions of particles in i'th and i+1'th degree of ionization, p_e - partial pressure of electrons, m_e - mass of the electron, h - Planck's constants, k - Boltzman's constant, T - temperature, ε_i - ionization energy for the i'th degree of ionization.

The expressions for n_{o+++} and n_e ($T > 4.5 \times 10^4$ °K) have been derived by the author by using a method similar to that used by Gross et al[20].

The thermal conductivity of the gas inside the bubble is now determined for a ten component mixture with the concentrations n_{H_2O}, n_{H_2}, n_{O_2}, n_H, n_O, n_{H+}, n_{O+}, n_{O++}, n_{O+++}, n_e as functions of the pressure p and temperature T. The method for calculating the thermal conductivity is again described by Gross et al[20] where the expression for the thermal conductivity κ_N is given by

$$\kappa_N = \sum_{i=1}^{k} \frac{n_i}{3} c_i \ell_i \left(\frac{5}{2} C_{i\,trans} + C_{i\,int}\right)$$

The thermal conductivity associated with the diffusion of dissociation (the diffusion of ionization is neglected) κ_D is given by

$$\kappa_D = \sum_{i=1}^{k} \frac{h_i \rho_i}{A} \left[\frac{\partial pM}{\partial T} \left(m_M - m_A \frac{\varepsilon_1}{\varepsilon_2}\right) - \frac{1}{n_i} \frac{\partial p_i}{\partial T}\right] +$$

$$+ \sum_{i=1}^{k} \frac{h_i \rho_i}{B} \left[\frac{\partial p_M}{\partial T} \left(m_M \frac{\varepsilon_1}{\varepsilon_2} - m_A\right) - \frac{1}{n_i} \frac{\partial p_i}{\partial T}\right]$$

where k - number of assumed components; c_i - mean thermal velocity, ℓ_i - mean free path, $C_{i\ trans}$ and $C_{i\ int}$ - specific heats of transitional and internal degrees of freedom for the i'th component, h_i - enthalpy of the i'th component, ρ_i - partial density of the i'th component, $A = n_M\varepsilon_1 + n_A\varepsilon_2$, $B = n_M\varepsilon_2 + n_A\varepsilon_3$, the indexes A and M refer to molecules and atoms respectively. The factors ε_1, ε_3, ε_2 represent the mutual collisions of molecules, atoms and atom-molecule collisions respectively.

The total thermal conductivity κ is given by

$$\kappa = \kappa_N + \kappa_D$$

Simplifying assumptions such as the neglect of the higher orders of ionization at low temperatures and the neglect of the influence of molecules and atoms at higher temperatures were made in the computation of κ.

2.7 The temperature distribution and heat outflow in the space between the plasma and the liquid

By assuming that the plasma column is described by the theory of a thermally inhomogeneous plasma column[17] (see also section 2.2), the temperature distribution in the space between plasma and liquid can be calculated. The temperature gradient in a cylindrical shell of a length l_c is:

$$\frac{dT}{dr} = -\frac{\dot{Q}}{2\pi l_c \kappa}$$

where $\dot{Q}$ - constant rate of heat outflow, T - temperature, r - radius, κ - thermal conductivity.

The direct integration of the above equation in the space between liquid and plasma is not possible because κ is a complicated

function of T (assuming the pressure P to be a constant). A numerical iteration technique must therefore be used to solve the boundary value problem defined by the temperature of the walls of the bubble and the plasma column.

The temperature distribution, the thermal conductivity and $\dot{Q}$ have been computed in Figure (2.13) for an approximation to the state existing at the end of a 100 μsec discharge shown in Figure (3.1a). For this case $\dot{Q} = 1.9 \times 10^8$ erg/sec. This can be compared with the energy of the oscillating bubble described in section 2.5 which has a kinetic energy of 1.05×10^3 erg and an oscillation period of 3.14 msec. The energy outflow during the first microsecond (assuming that temperature inside the bubble does not change) is comparable with the kinetic energy of the bubble. However, the temperature and therefore the heat outflow drop rapidly after the discharge extinguishes. Thus the exact solution of the behaviour of the cylindrical or spherical bubble after the end of the discharge requires the consideration of all thermal effects. This could be obtained by a numerical solution for the nonlinear partial differential equation.

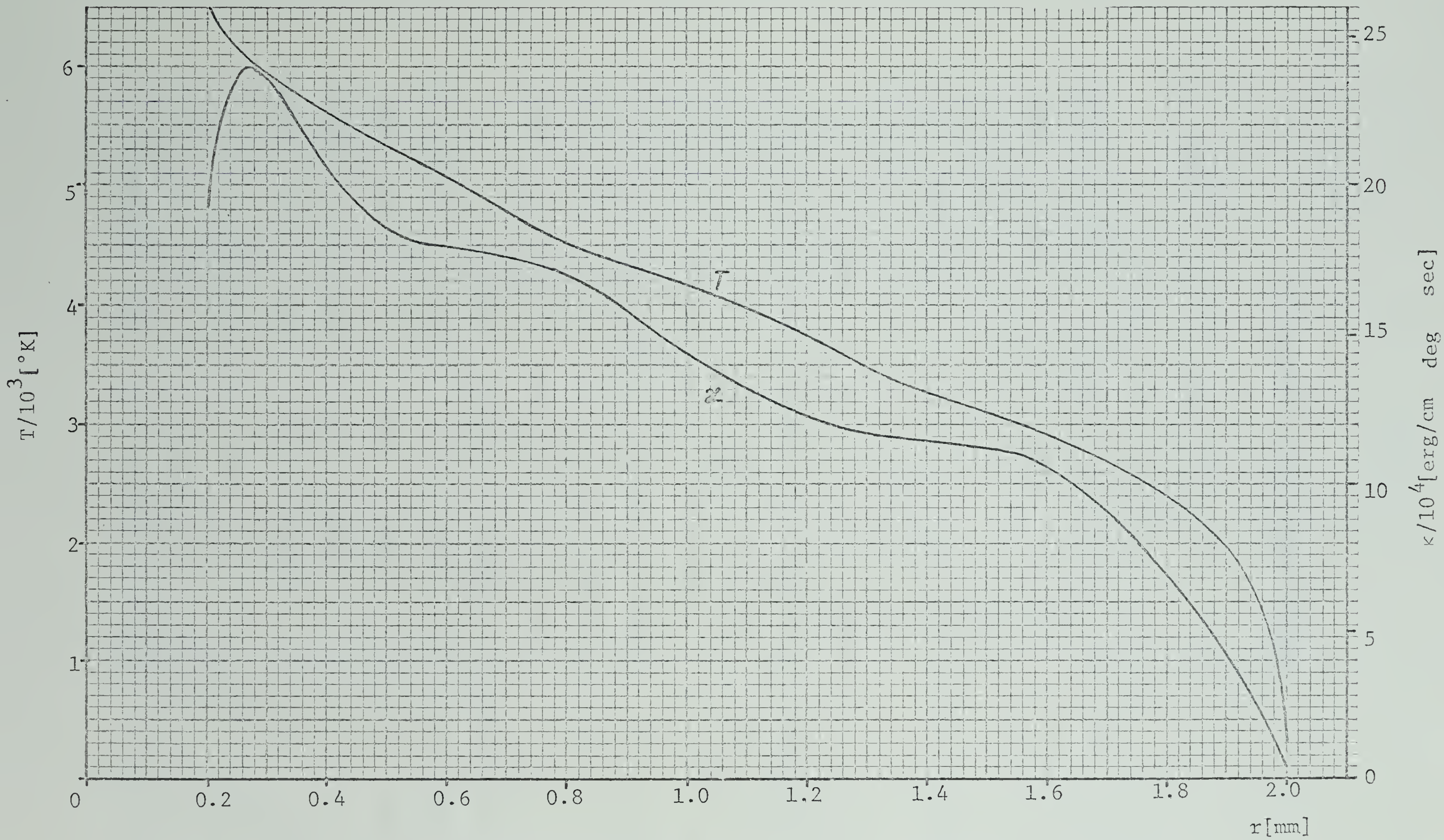

Fig. (2.13) The temperature T and the thermal conductivity κ in a gas shell. Calculations were made by assuming a plasma channel diameter of 0.4mm, a plasma wall temperature of 6.500°K, the bubble wall temperature equal to 300°K and a pressure of 0.1 atm in water.

CHAPTER 3

INSTABILITY OF THE PLASMA COLUMN

3.1 Unstable electrode phenomena

The presence of an electrode surface causes a cathodic sheath to appear at one end of the discharge column and a anodic sheath to appear at the other end. Each sheath has its mechanism characterized by a higher electric field intensity than that found in the remainder of the column and could under certain conditions influence the behaviour of the discharge column.

The motion and division of the cathodic spot has been observed for some time. However, the theoretical description of this phenomena has not been sufficiently developed. Because in many spark discharges the current density reaches values of up to 10^{12} amps/mm^2, some cathodic spot emission mechanism is probable. The extremely high emission current density in the cathodic spot cannot in all cases be explained by thermic or field emission.

The Longini's model[1] best explains the mechanism of cathodic spot emission. According to the Longini's model the very fast electrons disturb the upper layers of the cathode ion lattice in a fashion similar to that by ambipolar diffusion. A special transition layer is created by the cathodic material leaving the cathode with a metallic kind of electrical conductivity and a very low emission work function. According to Steenbeck's minimum principle the discharge current is concentrated at the cathodic spots. By using this principle it is also possible to

deduce that the number of cathodic spots is proportional to the current. The cathodic spots have been observed to move more or less at random on the surface of the cathode. The explanation of this motion is unfortunately unknown. A remarkable feature is that the stagnation of the spot leads to a slight increase in the cathodic voltage drop.

In some types of arcs, the current density is very unevenly distributed on the surface of the anode. This results in the current being collected by anodic spots which may sometimes be indistinguishable from cathodic spots.

The seige of the relaxation phenomena in the anodic region is commonly termed as "hash" by engineers. It occurs if the voltage drop in the anodic region is large. The anodic sheath is virtually short circuited by a plasma bridge, which is created by bursts of ionization.

3.2 Unstable column phenomena

Theoretical studies of the macroscopic instability of a plasma column in the presence of an external magnetic field have been made by Kadomtsev and Nedospasov[21], Hoh[22], Paulikes, Pyle[23], and Schmidt[24]. Instabilities similar to those studied in the case of an external magnetic field have been observed by Kocian[2] in the field free case. Similar instabilities were observed through the use of a time resolving camera by the author in discharges in a liquid, Figure 3.1b.

The instabilities of self pinched discharges are described by Cruzon[25], Wyld[26] and Kadomtsev[28]. Kadomtsev[28] gives the following criterion for the onset of the pinch instability:

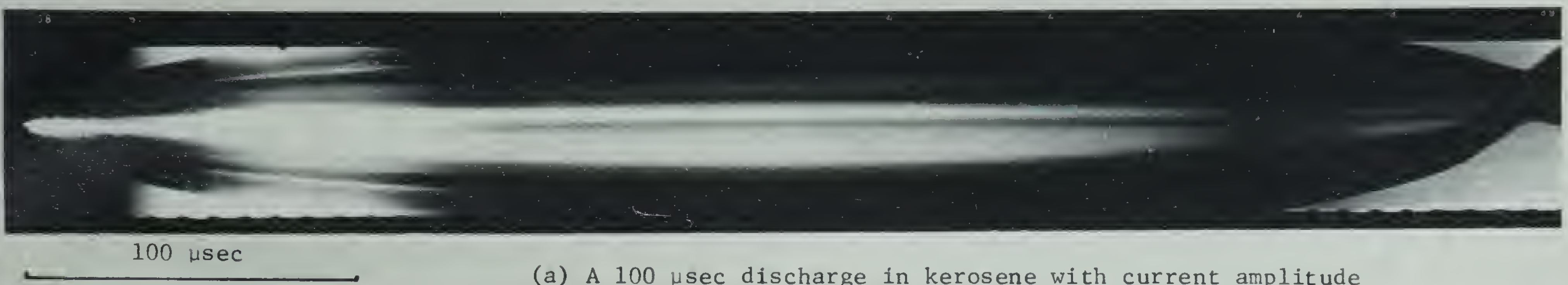

(a) A 100 µsec discharge in kerosene with current amplitude I_{dc} = 40 amp, and electrode distance d = 50 µ.

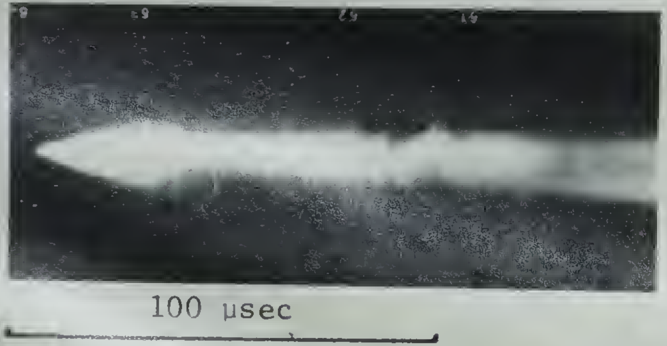

(b) 100 µsec discharge in kerosene with I_{dc} = 40 amp and d = 50 µ.

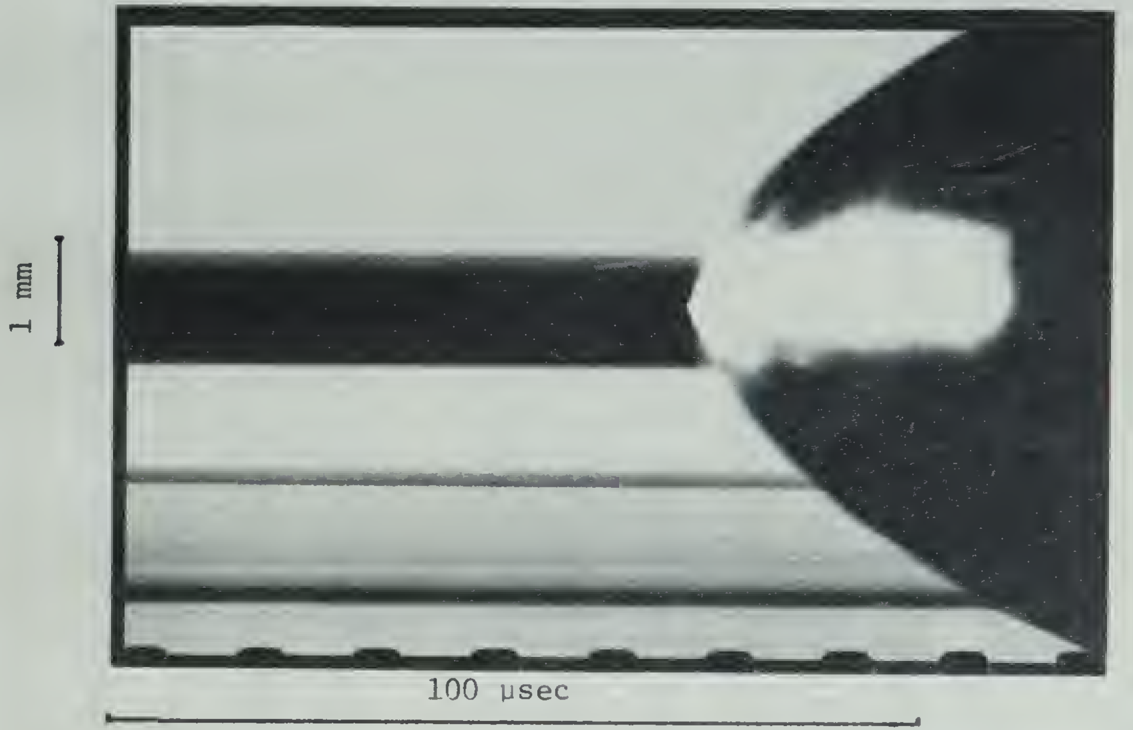

(c) 20 µsec discharge in water with I_{dc} = 100 amp and d = 50 µ.

Fig. (3.1) Records of discharges in liquids made by a time resolving camera

$$- \frac{d \ln p}{d \ln r} < \frac{48}{2+8\beta}$$

where $\beta = 8\pi p/B^2$ is the ratio of the plasma pressure to the magnetic pressure and the other symbols as described in the previous chapters.

The above conditions imply that for the pinch instability not to occur, the plasma pressure must not diminish too rapidly with increasing r (a condition well satisfied with the discharges under consideration). If the pressure falls off more rapidly, the pinch is unstable to an axially symmetric perturbation and a "necking" or "sausage" instability will occur.

Thermal instabilities are described by Kadomtsev[28] and by Ecker[18]. Kadomtsev[28] describes the case with an external magnetic field, while Ecker describes the field free case. In addition, Ecker describes the influence of the outer electrical circuitry on the instabilities. The essence of his theory which is based on the thermally inhomogeneous plasma column model[17] (see equations (2.4), (2.5), (2.6)) is as follows. A density disturbance produces a temperature disturbance. The temperature disturbance in turn results in a change of the ion production coefficient so that a coupling between the density and temperature exists. Secondly a density disturbance will cause a change in the longitudinal electric field. This too will influence the instability via the particle production and particle losses. The influence of the outer circuit is taken into account by the simple relation

$$U = I(\Omega_o + \Omega_i) = I\Omega_o + Elc \tag{3.2}$$

where U - constant voltage supply, Ω_o - outer resistance, Ω_i - resistance of the discharge, lc - column length and E - electrical field.

By using a first order theory to describe the perturbations in density and temperature which are assumed to propagate at a subsonic velocity, Ecker[18] obtains the following criterion for the onset of a thermal instability.

$$IE \geq 10\, \lambda_{oo} T_{oo} \frac{\sigma}{1 - 2\sigma} \qquad (3.3)$$

or

$$I_{cr} = \frac{10}{E} \lambda_{oo} T_{oo} \frac{\sigma}{1 - 2\sigma} \qquad (3.4)$$

$$\sigma = \frac{1}{1 + \frac{\Omega_i}{\Omega_o}} \qquad (3.5)$$

where I_{cr} - critical current, λ_{oo} and T_{oo} are heat conductivity and temperature within the Shottky approximation respectively.

Without an external resistance ($\sigma \to o$) the plasma column is always unstable. With increasing resistance ($\sigma \to 1$) the column is stabilized for currents below the critical value I_{cr}.

3.3 Other unstable phenomena

The exploding liquid and the vapourized metals streaming from the electrode surface can build up additional branches of the main channel. Traces of such branches have been observed on the polished electrode surface after a discharge in a liquid.

The vaporization of the electrode surface coupled with the irregularity of the moving liquid can cause the sudden changes of the pressure inside the gas bubble. A rough and irregular electrode surface in the proximity of the discharge can strengthen the above effect.

3.4 Correction of the thermal instability condition

From the thermal instability theory, the critical current I_{cr} is defined by equation (3.4). In this expression σ is assumed to be a constant. According to the formula (3.5) σ is a constant as far as the resistance of the discharge is constant. But from previous experiments, is known that the voltage on the spark gap is approximately constant for a very wide range of discharge currents. This will be further discussed in chapter 4. Thus the channel resistivity Ω_i is dependent on the current I. The following approximate relation for Ω therefore holds:

$$\Omega_i = \frac{1}{\beta I} \tag{3.6}$$

where β is a constant and from equation (3.5)

$$\sigma = \frac{\beta I \Omega_o}{1 + \beta I \Omega_o} \tag{3.7}$$

This gives

$$I_{cr} = \frac{10}{E} \lambda_{oo} T_{oo} \quad \frac{\beta I \Omega_o}{1 - \beta I \Omega_o} \tag{3.8}$$

or

$$I_{cr} = A \frac{\beta I \Omega_o}{1 - \beta I \Omega_o} \qquad \text{where} \quad A = \frac{10}{E} \lambda_{oo} T_{oo} \tag{3.9}$$

The cases where σ = constant and where $\sigma \neq$ constant are illustrated in Figure 3.2a and 3.2b respectively. In the case where σ = constant, a decrease in the current I results in a transition from the unstable region to the stable region (Fig. 3.2a). If the stabilizing character of the outer circuitry is preserved in the case where $\sigma \neq$ constant, a decrease in the current can lead to a transition from the stable to the unstable region (Fig. 3.2b).

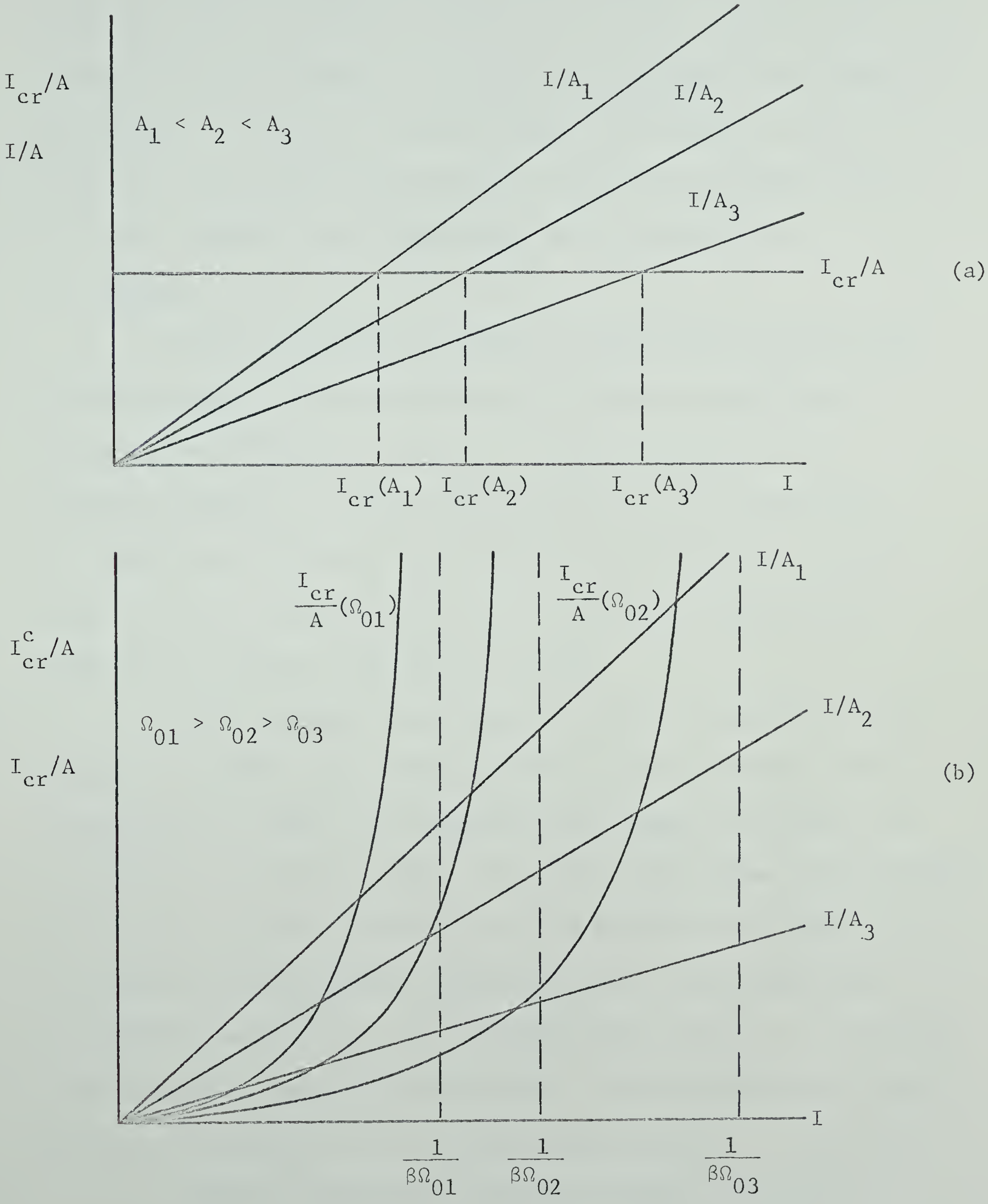

Fig. (3.2) The dependence of I_{cr} on I for

(a) σ = const

(b) $\sigma \neq$ const

As in the work by Ecker[10], the coefficient A in equations (3.4) and (3.9) is assumed constant, an assumption that does not always hold true. However, the object of the analysis is to show that indeed a transition from the stable to an unstable region is possible by decreasing the current I. The above conditions may be similarly applied to the higher modes of the instability.

3.5 Summary

From the previous chapters it follows that there are many possible reasons for the occurrence of discharge instabilities in liquids. The theoretical analysis of these instabilities is a difficult problem. In many cases not only are the instabilities not theoretically described as yet but the exact physical explanation of the discussed phenomena is not known, for instance the creation of a cathodic spot and its motion.

A more detailed experimental analysis is possible however. Figure 3.1 contains some records made by a time resolving camera of discharges in a liquid. The bunching which appears in Figure 3.1b is similar to a pinched column. The origin of the other irregularities may be due to thermal instabilities. The middle part of Figure 3.1b is similar to the "schlauch" instability (or a helix instability) described by Kocian[2] for a low pressure plasma column. The influence of the electrode phenomena is not clear. Unfortunately these records are not reproducible so that a more detailed analysis is impossible.

Further conclusions regarding discharge instabilities will be made after the description of the experiments which were performed to check the influence of the outer electrical circuitry, the geometric

arrangment and the liquid and electrode materials. For instance, in conjunction with the thermal instability theory, the effects of both the outer resistance damping and electrode phenomena will be investigated.

CHAPTER 4

EXPERIMENTAL RESULTS

4.1 Apparatus description and method of measurement

The spark gap consisted of two electrodes held by movable copper electrode holders, all of which were placed into a colorimetric cuvette filled with a liquid. A copper vessel with observation ports was placed into the cuvette to protect the cuvette against the strong shock waves created by the discharge in the spark gap. The spark gap area was illuminated from the rear side by a simple light source and was observed from the front side through a stereoscopic microscope. The microscopic ocular was equipped with a scale which allowed the direct measurement of the distance between the electrodes. The smallest measurable distance was 25 μm.

The spark gap was driven by a simple pulse independent EDM generator which is described in detail in Appendix A. An SCR connects the spark gap with a charged condenser through a load resistor. By making the time constant of this RC element sufficiently large, the current streaming through the spark gap could be assumed to be constant during a small portion of the discharge time. In the case considered the time constant $\tau = 2.7 \div 70$ msec and the observation time 20 μsec.

The inductance of the connection between the spark gap and the discharge condensor was minimized by using short thick wires in a parallel line arrangement. The total inductance of the discharge circuit was 0.713 μH thus giving a characteristic frequency of 12.7 kHz for the RLC circuit.

SCR's with a maximum turn on time of 3 μsec were sufficient for this experiment since the object of this study does not include the very fast phenomenon occurring at the outset and at the end of the discharge.

The discharge current and voltage were measured with a Tektronix 502 oscilloscope. The voltage on the spark gap was measured directly by the scope probe. The discharge current was measured on a shunt which was switched into the discharge circuit. The shunt comprised of a single wire with a resistance of 0.0775 Ω and an inductance of 2.1×10^{-8} Henrys. The shunt inductance was compensated for by the capacitor bridge in the probe used for measuring the shunt voltage. All electrical measurements on the discharge were made in the time interval between 60 and 80 μsec after the onset of the discharge. The maximum voltage to which the discharge capacitor could be charged was limited by the forward breakdown voltage of the SCR's. For the range of electrode distances that could be obtained, this voltage was insufficient for a pure liquid breakdown. This problem was solved by means of a tiny electrically conductive bridge which was built up between the two electrodes before the discharge. This bridge was created from a very small amount of graphite powder which was dispersed in the liquid. The single graphite particles were attracted by a weak electrical field into the maximal gradient space, where being polarized, attracted one other. The diameter of a graphite bridge formed in this way does not exceed few microns and its further influence is neglected.

In addition to the discharge current and voltage amplitudes and waveforms, the electrode distance, the value of the loading resistor

R_4 and the source voltage U_o were recorded. The evaluation of the current and voltage measurements was simplified by noting only the dc component and the average ac component amplitude in the interval 60÷80 μsec after the onset of the discharge.

Because of a large deviation in the values, each reading was repeated about 10 times and the average value calculated. All experiments were performed at room temperature (∿20°C) and 760 mm Hg pressure.

4.2 Liquid and electrode materials used

The number of required measurements grows rapidly with the number of liquids and electrode materials examined. In addition, the electrode distance, the discharge current and load resistor can be varied. Therefore the present investigation will only consider materials and parameters which may be readily obtained and described.

The following representatives of the main liquid groups were used in the experiments that were performed:

inorganic:	water and nitrogen
silicate:	silicon oil
organic:	benzene (cyclic hydrocarbon) and hexane (saturated hydrocarbon)

The most detailed measurements were made with water because water is a well defined substance, harmless, cheap and is relatively simple chemically. However, the conductivity of water is strongly enhanced even with a small amount of impurities such as CO_2 or NaCl. This results in a strong electrolytic effect during the formation of the graphite bridge. For this reason the water which was used was distilled, deionized and had the CO_2 removed by boiling. All metallic parts immersed in water were first passivated in HNO_3.

Liquid nitrogen was also used because of its very low temperature and chemical simplicity. The experiment was somewhat more complicated than that in which water was used because of the low temperature of the nitrogen. This necessitated the use of a metallic container with double observation windows as well as continuous compensation for the expansion of the electrode holders.

The chemically simple monoatomic inorganic liquids such as bromine were not used because of their poisonous nature.

Of the many types of silicon oils available, the use of the Dow Corning 705 diffusion pump oil (chemically a pentaphenyltrimethyltrisiloxane) was investigated. In addition to the presence of inorganic silicon in chemical bonds, a remarkable property of this liquid is a viscosity independent of temperature, over a wide range.

Benzene C_6H_6 and hexane $CH_3(CH_2)_4CH_3$ were used as the representatives of the cyclic and saturated hydrocarbons respectively. Mixtures of various liquid hydrocarbons are usually used in EDM.

Electrodes made from both copper and tungsten were tried. Differences in properties such as melting point, emission potential and thermal conductivity between these two materials allows an assessment of their influence on unstable electrode phenomenon.

The shape of the electrodes used was either that of a flat plate or a tip. The combination of two flat electrodes (corners on left electrode are rounded to eliminate edge effects) is shown in Figure 4.1a. A tip electrode is shown in Figure 4.1b.

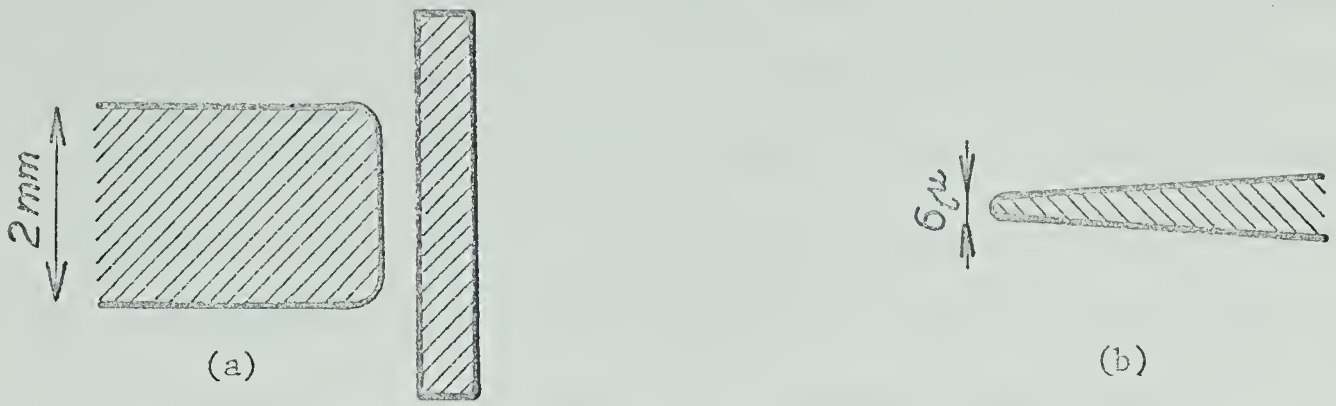

(a) (b)

Fig. (4.1) The shapes of electrodes

4.3 Experimental data

As discussed in chapter 3, the experimental investigation is limited to a characteristic case of interest to EDM. The flat Cu-Cu electrode combination in water was chosen as a basic configuration for reasons outlined in chapter 3.

Most of the experimental measurements were made on the basic configuration in which the electrode separation d, the source voltage U_o and the load resistor R_L were varied. For each case, values of the channel voltages (U_{dc} and U_{ac}) and the discharge currents (I_{dc} and I_{ac}), as they are defined in a typical record (Fig. 4.2) were measured.

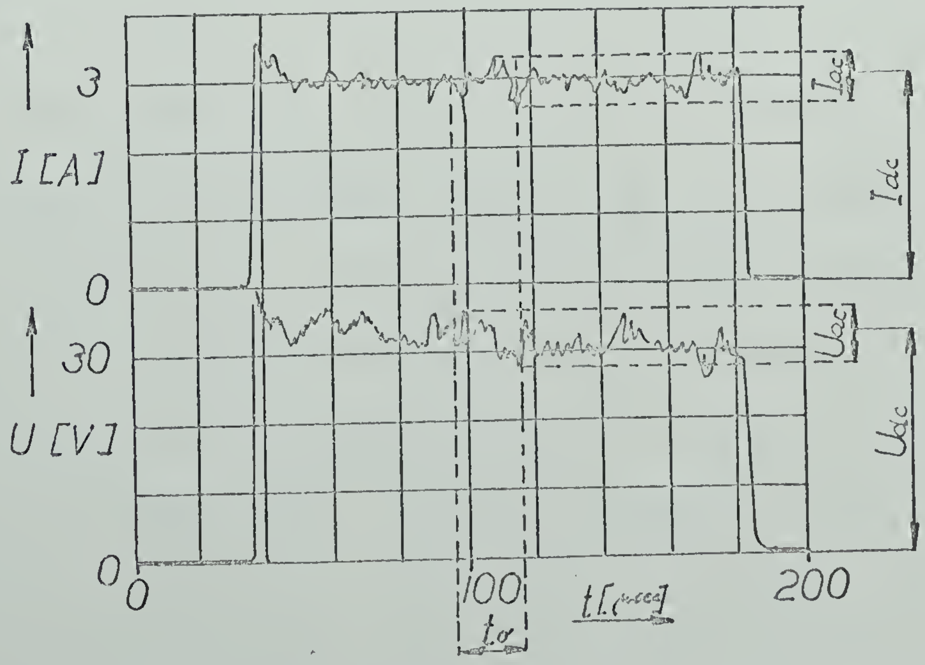

Fig. (4.2) The measured time dependence of U and I

With a load resistor larger than 200 Ω, a wide fluctuation in the measured values for I_{ac} was obtained. For this reason, the present analysis is restricted to smaller values for R_L. The typical dependence of I_{ac} on I_{dc} for R_L = 36 Ω is depicted in Figure (4.3). The influence of the electrode distance (for various values of R_L) on I_{ac} is slight. For this reason, the average measured value of I_{ac} (with the electrode separation in the range 25-100 μ) as a function of R_L is given in Figure (4.4). The stabilizing effect of the load resistor R_L as well as decrease of I_{ac} with an increasing I_{dc} is shown in Figure (4.4). The irregularity of the curve for R_L = 155 Ω is probably the result of the large deviations in the measured values.

Measurements with values of I_{dc} below 3 amperes were not made because of discharge interruptions as well as breakdown often not occurring at all.

The dependence of the voltage U_{dc} on the current I_{dc} is shown in Figure (4.5). From this figure, it may be seen that the assumption made in section (3.4) that the voltage U_{dc} is constant over a wide range of values for the discharge current I_{dc} is valid.

The voltage U_{dc} decreases with decreasing electrode distance. The dependence of the average values of U_{dc} on the electrode distance is shown in Figure (4.6). These curves are approximately straight lines with only a small dependence on R_L. By using the method of minimal squares, the average dependence of U_{dc} on d is given in Figure (4.6) (dotted line). The extrapolation of this line gives U_{dc} = 19.06 volts for d=0. This voltage represents the sum of the anodic and cathodic voltage drops. The slope of the average (dotted)

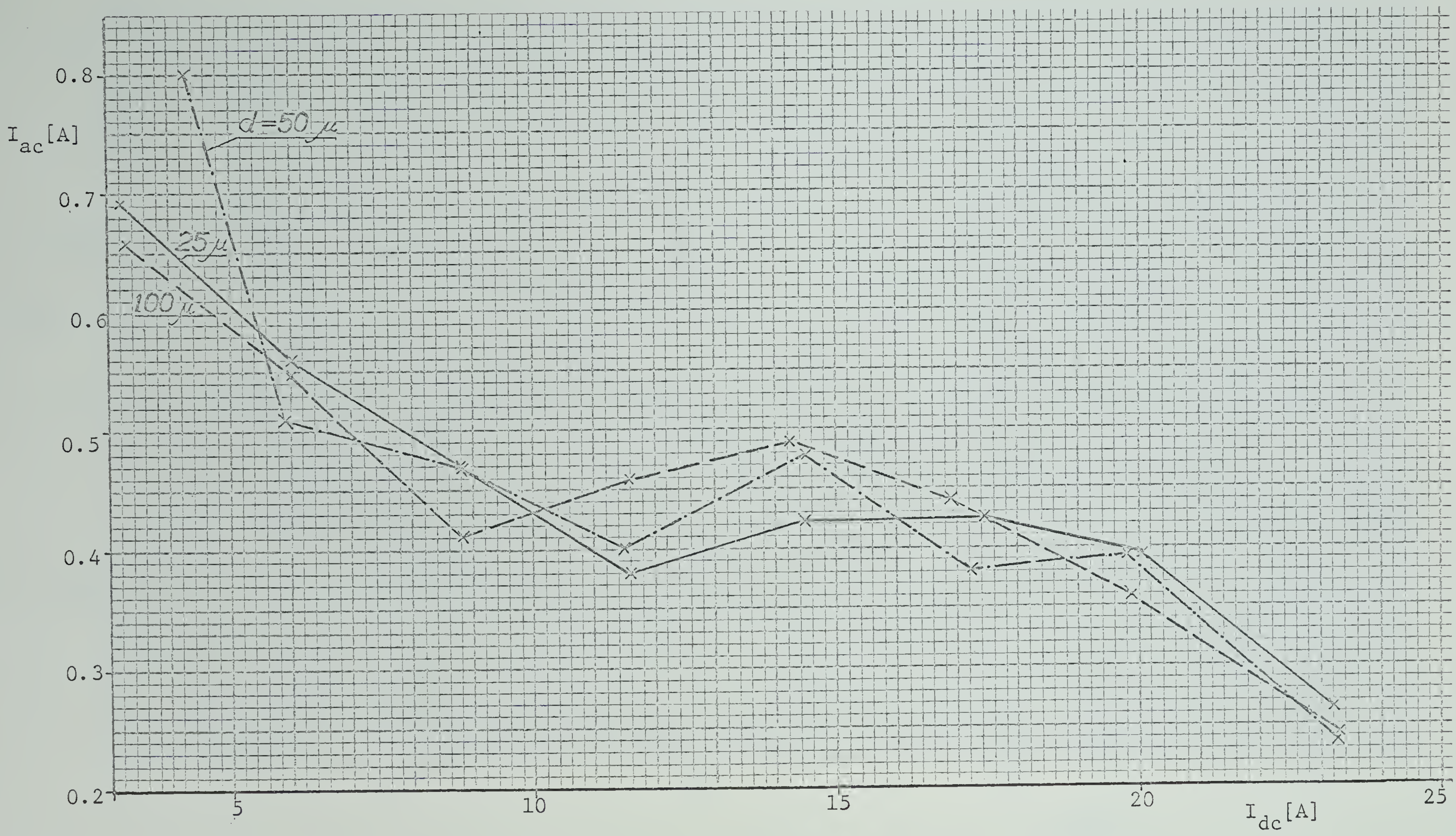

Fig. (4.3) The dependence of I_{ac} on I_{dc} for different electrode distances. The liquid dielectric is water, R_L = 36Ω and two flat Cu electrodes are used.

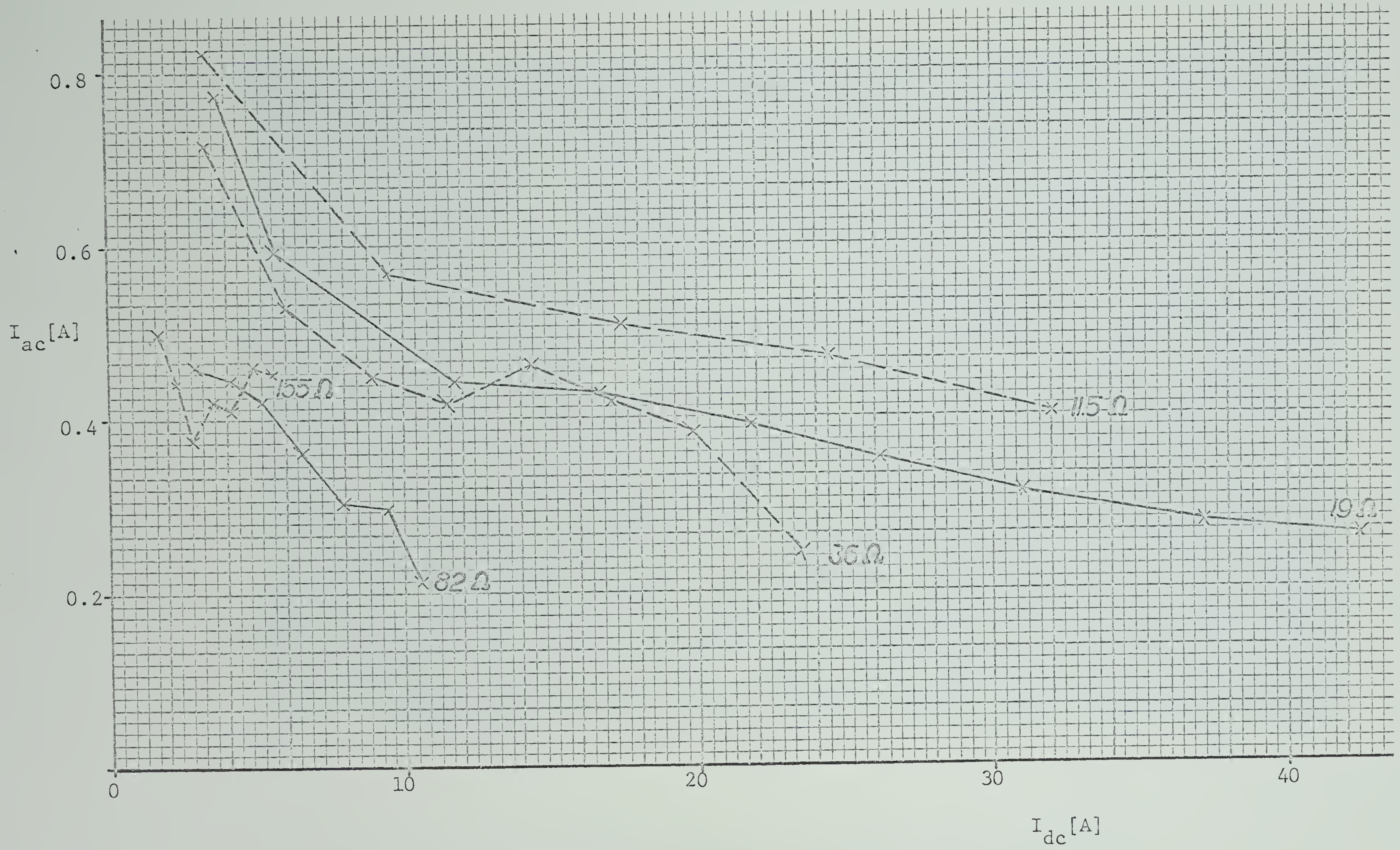

Fig. (4.4) The dependence of I_{ac} on I_{dc} for various values of R_L.
All other parameters are as given in Fig. 4.3.

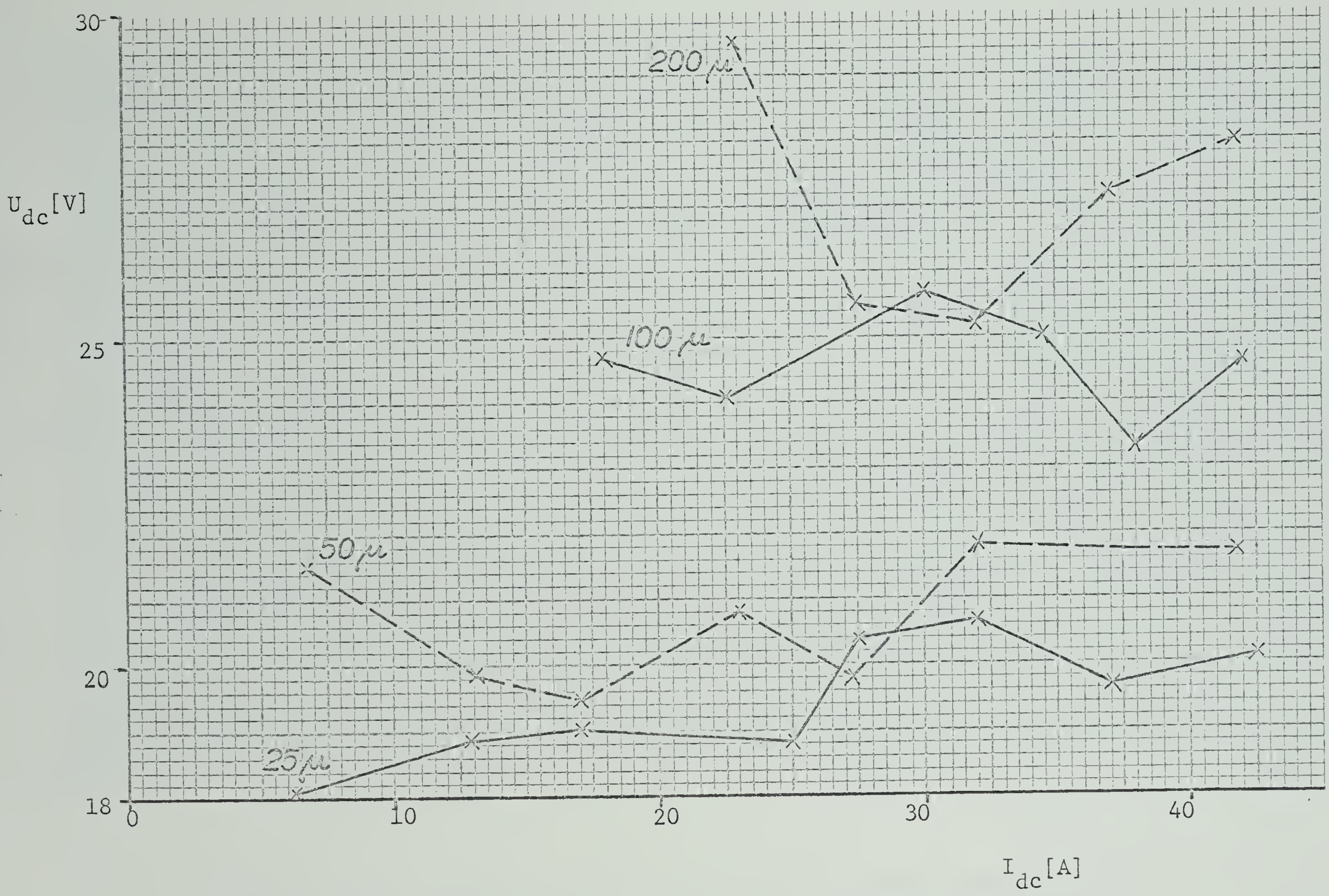

Fig. (4.5) The dependence of U_{dc} on I_{dc} for various values of d. All other parameters are as given in Fig. 4.3.

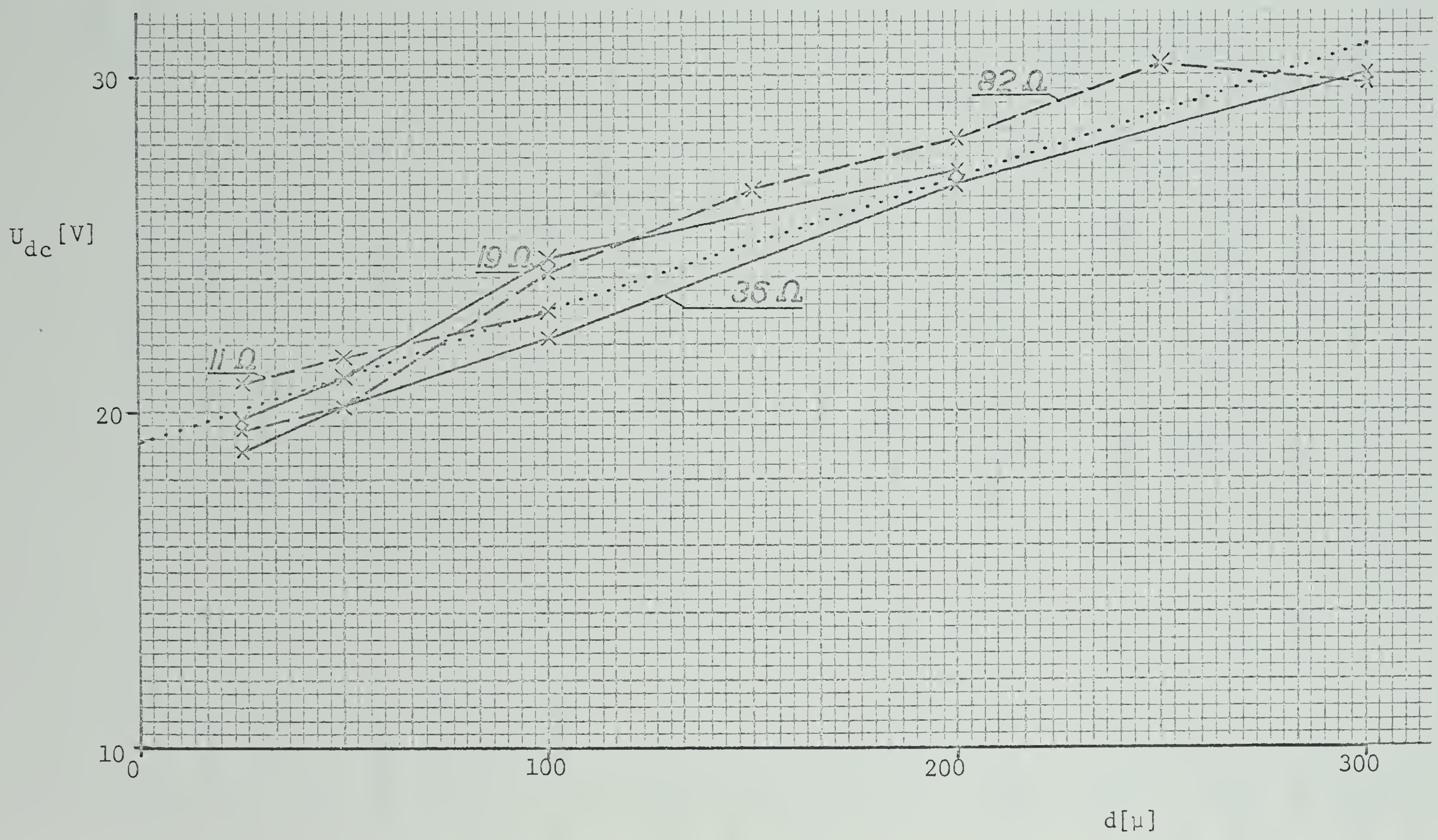

Fig. (4.6) The dependence of U_{dc} on the electrode distance d for different R_L. All other parameters are as given in Fig. 4.3.

line gives the electric field along the middle part of the discharge column, which in this case is E = 394.4 volts/cm. Because the slope of the measured curves does not change appreciably in the proximity of d = 25 μ (and they in fact must end in origin), the sum of cathodic and anodic sheath thicknesses must be less than 25 μ. (Measurements previously made by the author suggest a sheath thickness of about 5 μ). Thus the major portion of this discharge column is a axially homogeneous cylinder.

The dependence of I_{ac} on I_{dc} (where R_L = 19 and the flat Cu electrode distance d = 50 μ) for various liquids is shown in Figure (4.7). Of the liquids examined, the most unstable discharge occurred in water. The amplitude of I_{ac} is smallest in the case of a discharge in silicon oil and for currents I_{dc} greater than 30 amperes was less than the resolution of the measurement. The voltage characteristics of the liquids tested were practically identical with those of water in Figure (4.5).

The results of measurements with four different combinations of flat W and Cu electrodes (R_L = 19 Ω, d = 25 μ) in water are shown in Figure (4.8). In general, the stability of the discharge is reduced if one of the electrodes is made of tungsten. The discharge is less stable with the Cu_-W_+ combination than with the Cu_+W_- combination. Of the four combinations, the WW configuration is the most unstable.

The results of measurements with various combinations of shapes for the Cu electrodes (R_L = 19 Ω, d = 50 μ) in water are given below

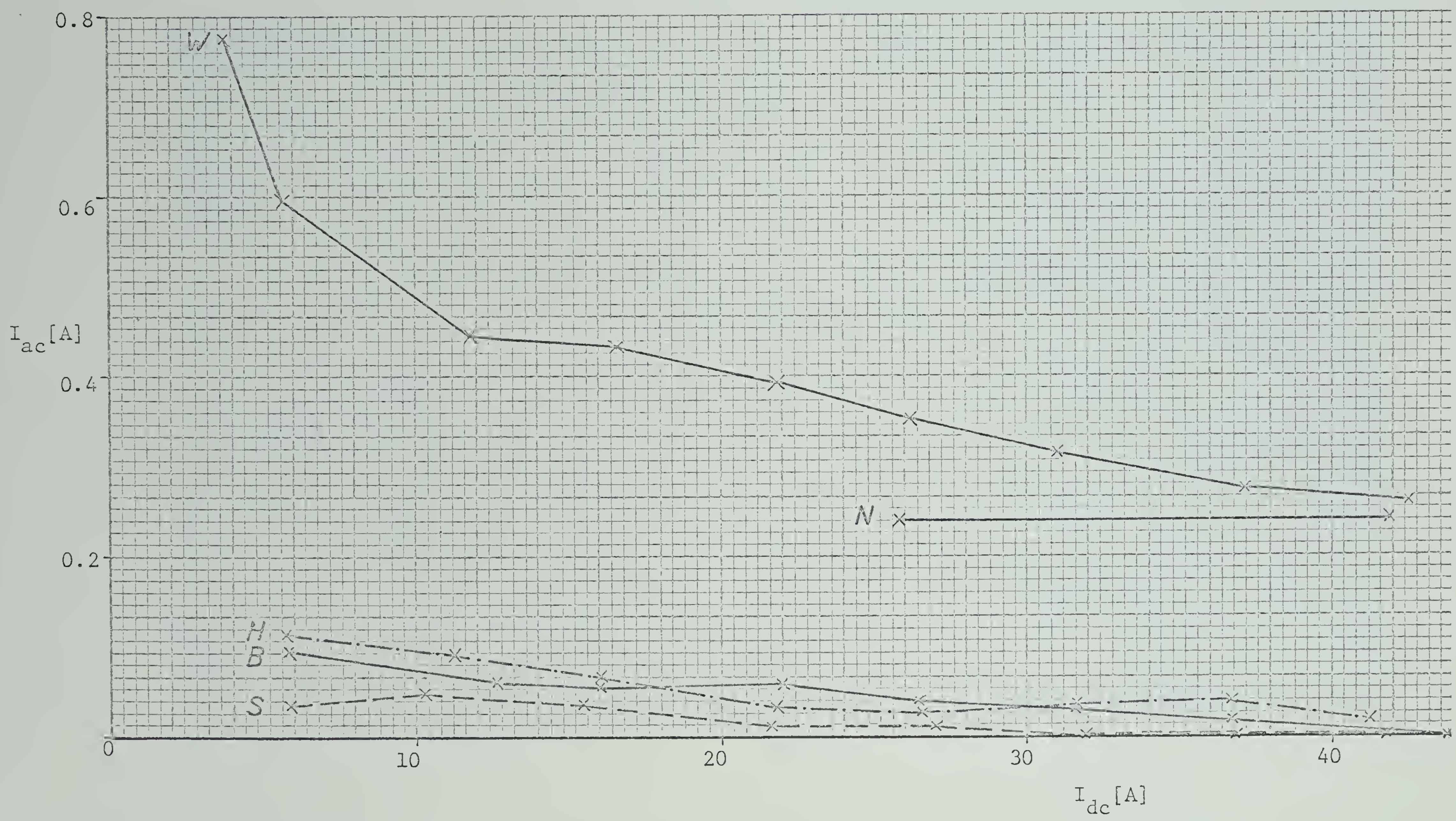

Fig. (4.7) The dependence of I_{ac} on I_{dc} for water (W), nitrogen (N), hexane (H), benzene (B), silicon oil (S). All other parameters are as given in Fig. 4.3.

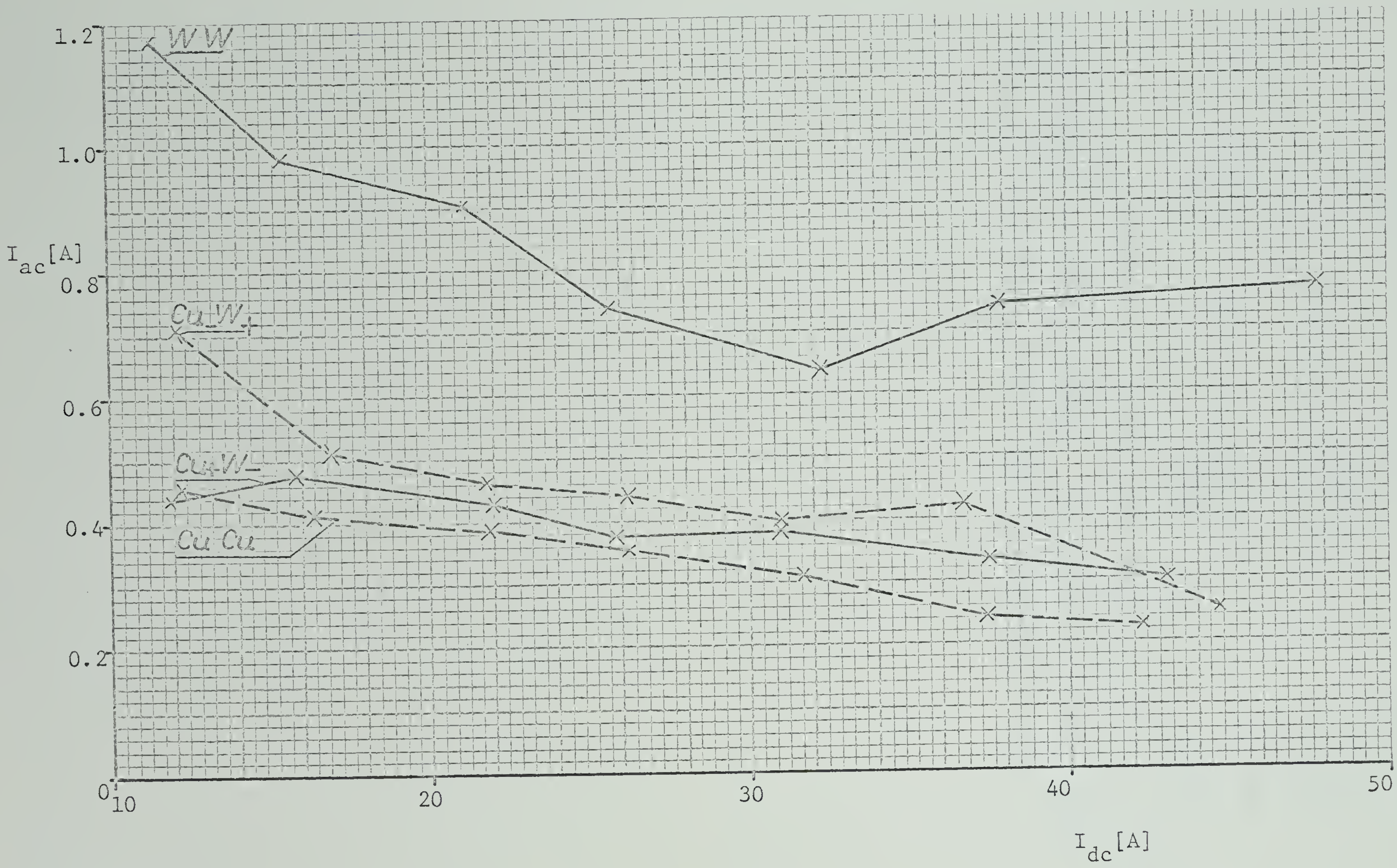

Fig. (4.8) The dependence of I_{ac} on I_{dc} for various Cu-W electrode combinations. All other parameters are as given in Fig. 4.3.

cathode	anode	I_{ac} [amp]
flat	flat	0.193
flat	tip	0.183
tip	tip	0.416
tip	flat	0.447

The increase of instabilities with a tip cathode, regardless of the shape of anode is evident. The slight difference between first and second combination could be due to experimental error.

CHAPTER 5

DISCUSSION AND SUMMARY

5.1 Discussion of theoretical investigation

One of the most important phenomena in EDM is the pressure in the discharge area. For this reason, a theoretical investigation has been made of the gas bubble oscillations after the discharge extinguishes. If the equation of motion together with the damping forces is known, the pressure which prevailed at the end of the discharge inside the bubble may be calculated from an optical record. Starting with a long impulse which is successively shortened, the pressure at the end of each discharge can be calculated. In this fashion the pressure profile for most of the length of discharge can be obtained.

In this thesis, the equation of motion of an ideal gas bubble oscillation has been derived. The agreement of such a description with experimental data is very good during the second half wave. (See Fig. 2.6 and 3.1a) The method for calculating frictional thermal energy losses has been extended. Thus a more accurate description of the bubble behaviour immediately after the discharge extinguishes is presented. A more detailed investigation of the actual shape of the gas bubble, which in fact is not an exact cylinder or sphere would further improve the accuracy of this method for calculating the pressure profile.

However, even if damping effects are neglected, the approximate calculation of the pressures inside the spark is still very valuable

because by noting that the pressure at the end of the discharge is relatively low (in Fig. (3.1a) it is 0.32 atm) and that the subsequent drop in pressure is gradual (minimum in Fig. (3.1a) is 0.085 atm), it may be concluded that the transport of material melted by the boiling mechanism occurs mainly during the discharge and not after the discharge extinguishes. This is in contrast to the mechanism occurring with relaxation generator EDM process.

5.2 Discussion of the experimental data and comparison with theory

The experimental data in chapter 4 represents over 4,000 measurements. The poor reproducibility of individual measurements necessitated a large number of measurements followed by a statistical evaluation. Even if the absolute values in this data are not considered as exact, the general behaviour of discharges in liquids are nevertheless still characterized.

The stabilizing effect of the load resistor R_L is evident in Figure (4.4) and in good agreement with the thermal instability theory (sections 3.3 and 3.4). Thus to reduce instabilities, a high power source voltage U_o with a large load resistor R_L is required. From the economic point of view this is not ideal since a large portion of the energy is lost in the load resistor R_L.

The enhancement of instabilities by low currents can also be explained by the thermal instability theory (section 3.4). The existence of other kinds of column instabilities, however, cannot be excluded on the basis of the experimental measurements made. A more detailed theoretical description as well as direct photographic and spectroscopic records are necessary for more accurate conclusions.

The electrode shape and material have a strong influence on the stability of the discharge. However, the influence of the electrode distance is slight. On the basis of the above phenomena it is possible to deduce that the observed instabilities are combinations of surface and column instabilities. The surface instabilities occur in a short part of the plasma column (shorter than 25 μ), but the voltage drop in this space (19 volts) represents an electric field which is higher than 7.5 kv/cm (previous measurements made by the author indicate a field of about 30 kv/cm). This would imply that even a small change in the discharge structure in this space would result in a considerable change in the discharge current. The enhancment of instabilities at low currents is probably due to a column instability (thermal instability) and is insensitive to the length of the discharge column because of the weak electric field present in the column.

The influence of the cathode shape on the discharge instabilities may be explained through the cathodic spot motion. If the cathodic spot moves on a sharp tip, the length of the current streamlines in the strong electric field are changed much more than if the spot moved on a flat electrode surface. The electrode material is probably responsible for the changes in the electric field structure in the proximity of the electrode surface, as well as influencing the motion of the cathodic spot.

The influence of the liquid used on the discharge instabilities is not clear. The calculation of the properties of substances such as silicon oil, benzene and hexane at high temperatures is a difficult problem. The structure of the plasma column and the gas shell as well

as the chemical reactions with the electrode surface can influence the stability of the discharge. The presence of carbon atoms in all three liquids (hexane, benzene, silicon oil) with small instabilities (see Fig. 4.7) is remarkable. In addition, the creation of carbides on the electrode surface in EDM in hydrocarbons has been observed. Thus some influence by the carbided electrode surface is possible. In addition, the very strong bonds in silicon oil cause the "bump" in the thermal conductivity (caused by the diffusion of dissociation energy) to appear much closer to the plasma column than in the case of water. Thus the shell of the hot neutral gas is smaller than that in water and the plasma column is situated in a "cold tube" where the possibility for its motion is now more restricted.

5.3 Summary

The problems which have been considered in this thesis are closely connected with practical applications of plasma discharges in industry. A complete and detailed solution to the problems has not been obtained because of the complexity of the mutually interacting phenomena.

However, valuable information, both quantitative and qualitative about the discharge dynamics and stability in liquids has been obtained, and an outline of the behaviour of independant generator discharges has been given. Techniques for the possible reduction of instabilities in EDM have been discussed. Finally, this thesis serves as a basis for the further theoretical and experimental research on discharges in liquid dielectrics.

BIBLIOGRAPHY

[1] Hoyaux, M.F., "Arc Physics", Springer-Verlag, New York Inc. 1968.

[2] Kocian, P., "Neve Untersuchungen uber Schlauchentladungen (New Investigations of "Schlauch" Discharges)", Zeitchrift fur Naturvorschung, 17a, 627, (1962).

[3] Skvortsov, Yu.V., Komelkov, V.S., Kuznetsov, N.M., "Expansion of a spark channel in a liquid," Soviet Physics-Technical Physics 5, 1100 (1960-61).

[4] Abramson, I.S., Gegechkori, N.M. Drabkina, S.I., Mandelshtam, S.L., "O kanale iskrovogo razrjada (About the spark discharge channel)" ZhETF 17, 862 (1947).

[5] Abramson, I.S., Gegechkori, N.M., "Oscilograficeskoje isledovanie iskrovogo razriada (The oscilographic observation of a spark discharge)", ZhETF, 21, 484 (1951).

[6] Drabkina, S.I., "K teorii razvitia kanala iskrovogo razriada (Contribution to the theory of a spark discharge)", ZhETF, 21, 473, (1951).

[7] Gegechkori, N.M., "Eksperimentalnoje isledovanie kanala iskrovogo razriada (The experimental observation of a spark discharge)," ZhETF, 21, 493, (1951).

[8] Brajinskii, S.I., "Theory of the development of a spark channel", Soviet Physics - JETP, 34, 1068, (1958).

[9] Andreev, S.I., Orlov, B.I., "Development of a spark discharge I", Soviet Physics - Technical Physics, 10, 1097, (1966).

[10] Andreev,S.I., Vanykov, M.P., Kotilov, A.B., "Growth of the spark discharge canal for a discharge circuit with a rapidly increasing current", Soviet Physics-Technical Physics, 7, 37, (1962).

[11] Egorova, V.F., Isaenko, V.I., Mak, A.A., Savykova, A.I., "Distribution of temperature and electron density in a spark discharge canal", Soviet Physics-Technical Physics, 7, 242, (1962).

[12] Jorn Koppitz, "Die radiale und axiale Entwicklung des Leuchtens in Funkenkanal untersucht mit einer Wischkamera (The radial and axial development of the radiation in the spark channel observed by timeresolving camera)", Zeitschrift fur Naturforschung, 22a, 1089, (1967).

[13] Tholl, H., "Spektroskopische Messung des Zeitliches Verlaufs der radialen Dichte – und Temperaturverteiligung in einem Wasserstoffunken (Spectral measurements of the time dependence of the radial density – and temperature distribution in a hydrogen spark)", Zeitschrift fur Naturforschung, 22a, 1068, (1967).

[14] Finklenburg, W., Maecker, H., "Elektrische Bogen und termisches Plasma (Electric arc and thermal plasma)", Handbuch der Physik Band XXII, Springer Verlag Berlin, 1956.

[15] Burz, G., Finklenburg, W., "Termische Lichtbogen hoher Temperature und niedriger Brennspannung (Thermal arc high temperature and low voltage)", Zeitschrift fur Physik, 138, 212 (1954).

[16] Burhorn, F., Maecker, H., "Feldstarkemessungen an wasserstabilisierten Hochleistungbogen (The Field strength measurements of water-stabilized power arc)", Zeitschrift fur Physik, 129, 369, (1951).

[17] Ecker, G., Zoller, O., "Thermally Inhomogeneous Plasma Column", Physics of Fluids, 7, 1996, (1964).

[18] Ecker, G., Kroll, W. Zoller, O., "Thermal Instability of the Plasma Column", Physics of Fluids, 7, 2001, (1964).

[19] Li Lam, Principles of Fluid Mechanics, Addison-Wesley, Inc., London, 1964.

[20] Gross, B., Gryez, B., Mikloszy, K., Plasma Technology, ILIFFE Books Ltd., London 1968.

[21] Kadomtsev, B.B., Nedospasov, A.V., "Instability of the Positive Column in Magnetic Field and the "Anomalous" Diffusion Effect", Journal of Nuclear Energy (part C), 1, (1959-1960).

[22] Hoh, F.C., "Screw Instability of a Plasma Column", Physics of Fluids, 5, 22, (1962).

[23] Paulikes, G.A., Pyle, R.V., "Microscopic Instability of the Positive Column in a Magnetic Field". Physics of Fluids, 5, 348, (1962).

[24] Schmidt, G., "Rotation of Plasmas in Pinches", Physics of Fluids, 5, 636, (1962).

[25] Curzon, F.L., Lotham, R., Nihon, J.A., "Experiments on the Growth Rate of Surface Instabilities in a Linear Pinched Discharges", Society of London Proceedings, A257, 386, (1960).

[26] Wyld, H.W., "Dynamics Stability of a Self-Pinched Discharge", Journal of Applied Physics, 29, 1460, (1958).

[27] Kadomtsev, B.B., "Hydromagnetic Stability of a Plasma", Reviews of Plasma Physics.

APPENDIX A

DESCRIPTION OF THE IMPULSE GENERATOR

The schematic of the impulse generator is given in Figure (A.1). The generator is able to produce single power impulses with approximately rectangularly shaped current impulses for discharges in the spark gap G. The power circuit consisting of a power capacitor C_1, loading resistor R_4, switching SCR S_1, extinguishing capacitor C_2 and extinguishing SCR's S_2 and S_3, is controlled by a time delay pulse generator with SCR's S_4 and S_5 manually controlled by the push botton switch PBS. In the rest state, switch PBS is disconnected and SCR's S_4 and S_5 are opened. If PBS is closed, SCR S_4 closes, and capacitor C_7 is quickly discharged through the transformer T_1 into the larger capacitor $C_{10...13}$. The secondary coil of the transformer T_1 induces a sharp impulse which is damped by resistor R_{13} and used for closing SCR S_1. Capacitor C_8 is simultaneously discharged through the capacitor C_8. Thus the voltage on the capacitor $C_{10...13}$ rises according to the time constant of the combination of $C_{10...13}$, C_8, R_{23}. When this voltage (limited by the zenner diode D_5) is high enough, SCR S_5 closes and capacitor C_9 discharges, creating two time delayed impulses in the secondary coils of the transformer T_2. After capacitors C_7, C_8 and C_9 discharge through the SCR's S_4 and S_5, the capacitors C_7, C_8, C_9 slowly charge again through high resistors R_{17}, R_{18}, R_{19}. Capacitor $C_{10...13}$ discharges through resistor R_{24} and the variable time delay circuit returns the initial state. Time delays

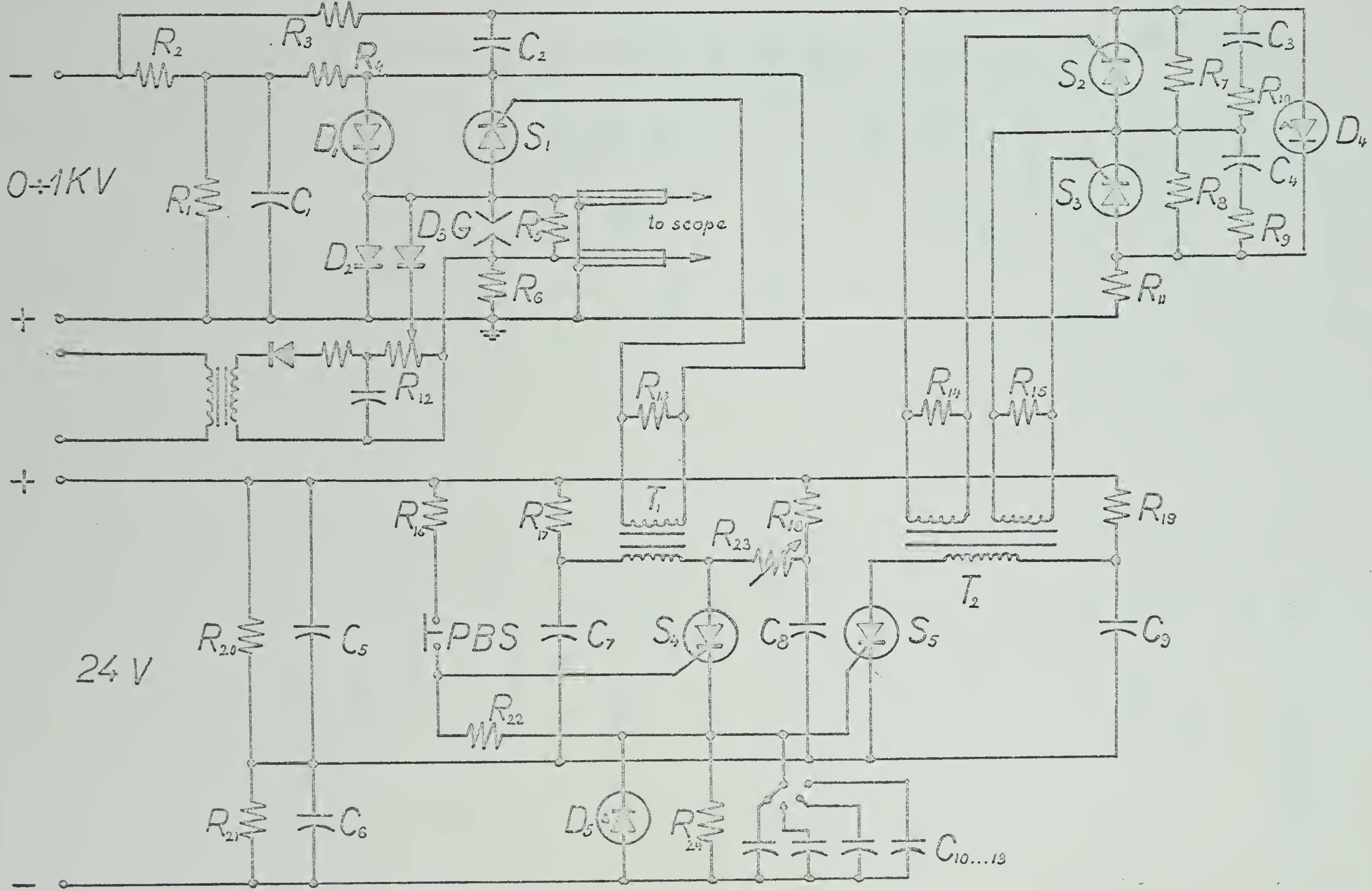

Fig. (A.1) Schematic Diagram for the impulse generator.

$R_1 = 100$ kΩ
$R_2 = 15$ kΩ
$R_3 = 27$ kΩ
$R_4 = 11 \div 350$ Ω
$R_5 = 2{,}2$ kΩ
$R_6 = 0.0662$ Ω
$R_7 = R_8 = 220$ kΩ
$R_9 = R_{10} = 4.5$ Ω
$R_{11} = 0.5$ Ω
$R_{12} = 1$ kΩ
$R_{13} = R_{14} = R_{15} = 15$ Ω
$R_{16} = 1$ kΩ
$R_{17} = R_{18} = R_{19} = 100$ kΩ
$R_{20} = R_{21} = 150$ Ω
$R_{22} = 200$ Ω
$R_{23} = 150$ Ω
$R_{24} = 22$ kΩ

$C_1 = 237$ μF (≤ 0.035 μH)
$C_2 = 28$ μF
$C_3 = C_4 = 0.33$ μF
$C_5 = C_6 = 100$ μF
$C_7 = 0.5$ μF
$C_8 = 20$ μF
$C_9 = 0.5$ μF
$C_{10} = 5$ μF
$C_{11} = 10$ μF
$C_{12} = 15$ μF
$C_{13} = 20$ μF

D_1 = 1N4508
$D_2 = D_3$ = 5A10D
D_4 = 1N4508
D_5 = 1ZM1575

S_1 = 16RC100A
$S_2 = S_3$ = 16RC60A
$S_4 = S_5$ = MCR1906-2

in the range of 10 μsec to 1 msec may be obtained by switching between capacitors $C_{10...13}$. A fine regulation of the time delay is provided by potentiometer R_{23}.

In the power circuit all SCR's are open in the initial state. The power capacitor C_1 and the extinguishing capacitor C_2 are charged. The starting impulse from transformer T_1 closes the SCR and capacitor C_1 slowly discharges (because large value of R_5) through R_4, S_1 R_5, R_6 until the breakdown in the spark gap G occurs. The time delayed impulses from transformer T_2 close the extinguishing SCR's S_2 and S_3 and the extinguishing capacitor discharges through S_2, S_3, R_{11}, D_2, S_1 as long as S_1 is closed. When no current is streaming through SCR's S_2 and S_3, these open spontaneously. After the discharge extinguishes, capacitors C_1 and C_2 charge slowly through resistors R_2 and R_3 respectively and all circuits return to the initial state. The power SCR's are protected against overvoltage by avalanche diodes D_1 and D_4. The non-equal reverse current of SCR's S_2 and S_3 is compensated for by resistors R_1 and R_8. The difference between their dynamic characteristics is compensated by C_3, R_{10}. C_4, R_9. The extinguishing current peak is limited by R_4. The electric field which is necessary for the creation of a graphite bridge is provided by the dc voltage source connected across the gap G through diode D_3. Two SCR's are used in the extinguishing circuit because of the higher inverse voltage peaks that encountered. Only one SCR is necessary in the main circuit.

B29964